RSC Advances

PAPER

View Article Online
View Journal | View Issue

Cite this: *RSC Adv.*, 2025, **15**, 33189

Toxic crystal violet dye removal by novel, eco-friendly seablite biochar–ferrite composite: adsorption isotherm, kinetics, and artificial neural network

Disha Mehta,[a] Pragnesh N. Dave *[a] and V. Vijay Kumar[b]

Rising water demand has intensified pollution and created an urgent need for efficient treatment methods. Adsorption is a green and low-cost approach, yet conventional adsorbents often face sustainability and regeneration challenges. In this study, a novel adsorbent was developed by pyrolyzing *Suaeda monoica* leaf powder (LP) into biochar (BC300), followed by base treatment and coprecipitation with $NiCuZnFe_2O_4$ spinel to form a ferrite–biochar composite (FCOB). FCOB effectively removed Crystal Violet (CV) dye from aqueous solution. FE-SEM images revealed a layered morphology, while FTIR analysis confirmed multiple adsorption mechanisms, including hydrogen bonding, electrostatic attraction, surface complexation, and pore filling for CV adsorption. Optimization studies showed maximum CV removal at pH 8 with a 30 mg FCOB dose, maintaining >95% removal up to 200 mg L^{-1} dye concentration. For higher concentrations, 150, 250 mg L^{-1}, the equilibrium time was 120 min. The Langmuir model indicated monolayer adsorption with a maximum capacity (q_{max}) of 325.5 mg g^{-1} at 30 °C, whereas the Dubinin–Radushkevich (D–R) model (E < 8 kJ mol^{-1}) suggested physical adsorption. Kinetic analysis revealed that the pseudo-second-order (PSO) model best described the process, indicating the chemical nature of CV adsorption onto FCOB, while the Elovich model provided a better fit at higher concentrations, reflecting surface heterogeneity. Thermodynamic parameters confirmed that CV adsorption was spontaneous and endothermic ($\Delta H°$ = 49.03 kJ mol^{-1}). FCOB retained >275 mg g^{-1} capacity after five regeneration cycles, demonstrating good reusability. Artificial neural network (ANN) modeling reliably predicted adsorption performance (R^2 > 0.99) using pH, dye concentration, dose, time, and temperature as inputs. These findings highlight FCOB as an economical, eco-friendly, and scalable adsorbent for dye removal from wastewater.

Received 30th June 2025
Accepted 5th September 2025

DOI: 10.1039/d5ra04604a

rsc.li/rsc-advances

1. Introduction

Crystal violet (CV), also known as methyl violet 10B or gentian violet, is a cationic triphenylmethane dye ($C_{25}H_{30}N_3Cl$).[1] In solid form, it appears dark green, but in water or ethanol it turns deep blue-violet with an absorbance maximum at 590 nm (ε = 87 000 L mol^{-1} cm^{-1}). CV is widely used as a pH indicator, in textile dyeing, gram staining, histology, antimicrobial applications, and fingerprint detection due to its strong binding to negatively charged surfaces.[2] Thus, it is a multipurpose dye.

CV dye is widely used but potentially toxic, exhibiting carcinogenic, mutagenic, and cytotoxic effects, and can harm the skin, eyes, liver, kidneys, and respiratory system.[1,3] As a recalcitrant dye, CV persists in water, bioaccumulates in aquatic organisms, and contributes to environmental pollution, deteriorating water quality. With the world population estimated at ~8.2 billion in August 2025 and projected to reach 9.7 billion by 2050, the demand for clean, potable water is increasing, making the removal of CV essential to protect human health and ensure sustainable water availability.[4]

There are various techniques (*e.g.*, chemical, biological, physical) for treating CV dye from wastewater. Chemical treatment methods (*e.g.*, AOPs-Advanced Oxidation Processes like Fenton, ozonation, and photocatalytic reactions) can effectively degrade or remove CV dye, but they often involve high operational costs, energy demand, and secondary pollution.[5,6] Several biological techniques are biosorption, algae, anaerobic and aerobic, fungal, bacterial, and enzymatic.[7,8] The main disadvantages of biological treatment are the large land area and long retention time required, along with its sensitivity to temperature, pH, toxicity, and shock loads that affect process stability.[9] Various physical methods are adsorption, sedimentation, flotation, membrane filtration, and flocculation.[10–12] These methods are simple, cost-effective, and easy to operate.

[a]*Department of Chemistry, Sardar Patel University, Vallabh Vidyanagar, 388 120, Gujarat, India. E-mail: pragnesh7@yahoo.com*
[b]*Gujarat Institute of Desert Ecology, Bhuj-370 001, Gujarat, India*

Although among the various techniques mentioned for the removal of CV dye from wastewater, only a few are generally employed at the industrial level for technological and remunerative reasons.[13] Among all the mentioned treatment approaches, adsorption is widely used because of its simplicity, low cost, high effectiveness, and environmental friendliness.[14] As it can be used for a wide range of contaminants, the process can be tailored for specific contaminants through the use of appropriate adsorbent modifications. The use of natural or waste-derived materials as adsorbents further promotes sustainability, while their regeneration potential helps minimize long-term costs. For instance, NaOH-activated avocado shell adsorbents achieved 96.9% CV removal with a capacity of 179.8 mg g^{-1}, GO–SO_3H exhibited an adsorption capacity of 202 mg g^{-1} for CV, while *Urtica dioica* leaf powder removed 93.68% of CV with a capacity of 312.5 mg g^{-1}.[15–17] Therefore, adsorption has a great potential for CV removal from wastewater.

A wide range of adsorbent materials is utilized to effectively remove dyestuffs from wastewater. Researchers continue to strive for superior options in terms of performance and eco-friendliness. While adsorbents are often derived from environmentally friendly materials, some are still produced from less sustainable and toxic sources due to their supreme adsorption efficiency.[18] For example, Mi Xiao *et al.* synthesized Cd-MOF, which effectively removed cationic dye methylene blue (MB) with a high adsorption capacity value of 595.4 mg g^{-1}.[19] Nevertheless, the heavy metal Cd is utilized in MOF, which negatively affects the environment being highly toxic.

Although activated carbon is a widely used adsorbent, issues including high manufacturing costs, poor selectivity, environmental concerns, and difficulties with regeneration and reuse frequently limit its efficacy.[20] Biochar has recently emerged as a sustainable alternative to activated carbon, offering lower cost, reduced energy demand, adequate adsorption capacity, and a smaller environmental footprint. Biochar is a carbon-rich material produced by pyrolyzing (300 °C to 900 °C) biomass under oxygen-limited conditions.[21] It is commonly derived from agricultural residues, forestry waste, or animal manure, with pyrolysis conditions determining its properties and adsorption efficiency.

The coupling of ferrite spinels with biochar is increasingly regarded as a novel and efficient approach for enhancing adsorption capacity in wastewater treatment applications, *i.e.*, biochar coated with magnetic Fe_3O_4 nanoparticles (MBC) showed higher adsorption capacity (99.19 mg g^{-1}) for CV dye than that of pristine biochar (80.36 mg g^{-1}).[22] Ferrite spinels (MFe_2O_4, where M = divalent cations such as Ni, Co, Zn, Cu, Mg, or Mn) are transition metal oxides with flexible cation distribution in tetrahedral and octahedral sites, forming normal or inverse structures.[23–25] They exhibit strong magnetism, chemical stability, tunable surface chemistry, and ease of modification, which make them useful in catalysis, energy storage, and environmental applications. Recently, biochar–ferrite composites have been increasingly used in wastewater treatment because they combine the advantages of both materials.[26] Biochar offers a porous, low-cost, and stable support, while ferrites provide magnetic properties, chemical stability, and additional reactive sites. This synergy enhances adsorption through ion exchange, complexation, and redox processes. Their magnetic properties simplify the recovery process of used adsorbent after multiple cycles.[27]

Suaeda monoica is a halophytic plant belonging to the Chenopodium family, commonly distributed in saline and coastal regions of Gujarat, Rajasthan, Tamil Nadu, and Andhra Pradesh in India.[28] It thrives under extreme salinity and drought, and its biomass is inherently rich in lignocellulosic matter, minerals, and functional groups, making it a promising precursor for biochar synthesis. *Suaeda monoica* is known for its medicinal and ecological applications, yet its role in water remediation remains underexplored.

In the present work, a novel FCOB adsorbent is reported for the removal of CV dye. The comprehensive physicochemical characterizations were performed to understand the structural and surface features of the FCOB adsorbent. The adsorption of CV onto FCOB was evaluated under varying conditions, and its efficiency was assessed through isotherm, kinetic, and thermodynamic analyses. In addition, an artificial neural network (ANN) model was employed to predict adsorption performance and to complement the experimental results. This work presents the first report on the synthesis of modified *Suaeda monoica* biochar (FCOB) and its application for the removal of toxic CV dye. The prepared adsorbent is therefore novel and distinctive, offering a valuable contribution to the development of advanced adsorbent materials.

2. Experimental

2.1. Materials

The adsorbate-crystal violet (CV) or gentian violet-$C_{25}H_{30}N_3Cl$ is from Merck pharmaceutical company. Its chemical structure is given in the chemicals that were used for the preparation of the adsorbent-FCOB were: (1) copper dinitrate trihydrate ($Cu(NO_3)_2 \cdot 3H_2O$) from Merck having ≥99% purity, (2) nickel dinitrate hexahydrate ($Ni(NO_3)_2 \cdot 6H_2O$) from SRL having 99% purity, (3) zinc dinitrate hexahydrate ($Zn(NO_3)_2 \cdot 6H_2O$) from SRL having minimum 99% from HiMedia having purity of 98 to 100%, (4) iron trinitrate nonahydrate ($Fe(NO_3)_3 \cdot 9H_2O$), and (5) sodium hydroxide (NaOH) pellets AR from Samir Tech with purity of 99%. HCl (35.4%) that was used to adjust the pH during adsorption experiment was from Loba Chemie manufactures. NaOH was used in CV dye adsorption experiment too. All these chemicals were used without purification or treatment. Distillery machine was used to produce distilled water from tap water in the laboratory. To ensure purity, only distilled water was utilised for the whole experiment.

Suaeda monoica was gathered from National Highway 141, Kandla Port Road, near Gulf of Kutch, Gandhidham, Kutch, Gujarat (370210), India. GPS coordinates of this address are 23.026266°N 70.191478°E. Images of *Suaeda monoica* plant location site, and dried plant are shown in Fig. S1.

2.2. Synthesis of FCOB adsorbent

Leaves of *Suaeda monoica* (LP) were washed thoroughly with distilled water, dried under sunlight for one week, and ground

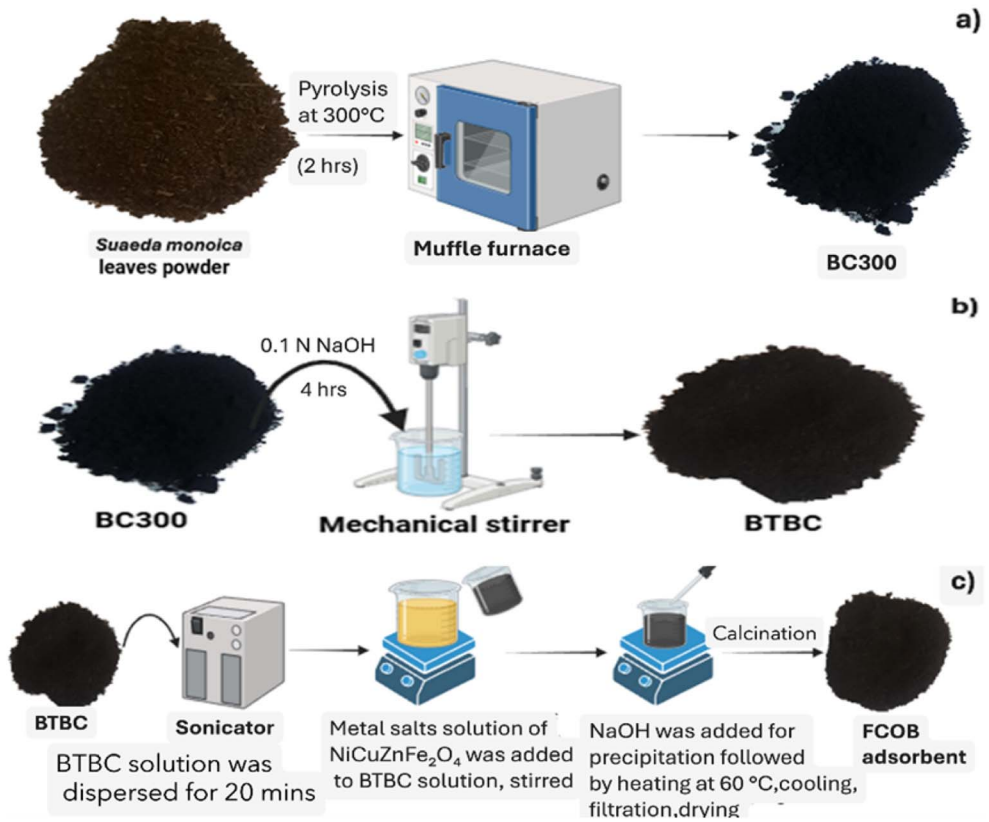

Fig. 1 Synthesis of FCOB adsorbent.

into fine powder. The pyrolysis of 20 g LP was done in a muffle furnace at a constant temperature of 300 °C in the absence of oxygen. It was carried out for 2 h at a heating rate of 2.5 °C min^{-1} to obtain biochar-BC300. The resulting BC300 weighed 13.1 g (65.5% yield). BC300 was kept in oven for 24 h and then stored in an airtight sample container.

13.1 g BC300 was immersed in 1310 mL of 0.1 N NaOH (13 pH) and mechanically stirred for 4 h. It was further filtered and repeatedly cleaned with distilled water. The resulting black alkaline precipitates of BC300 were marked as BTBC. BTBC was dried in an oven overnight and stored in a tight container.

In total, four FCOB composites were obtained by combining BTBC with $NiCuZnFe_2O_4$ in different weight ratios (see SI-Section S1, Table S1). Among all the composites, FS3 with a 2 : 1 ratio of BTBC to $NiCuZnFe_2O_4$ showed the best performance (refer Section 3.8.1) and was therefore chosen for bulk synthesis. The adsorbent FCOB (FS3) was synthesized *via* coprecipitation method as follows: (1) pre-calculated moles of metal nitrate salts $Fe(NO_3)_3 \cdot 9H_2O$ (0.02752 moles), $Ni(NO_3)_2 \cdot 6H_2O$ (0.01376 moles), $Cu(NO_3)_2 \cdot 3H_2O$, (0.01376 moles) and $Zn(NO_3)_2 \cdot 6H_2O$ (0.01376) were dissolved in 100 mL distilled water and stirred for 30 minutes to make homogeneous solution. (2) 60 mL of distilled water was added to 10 g of BTBC in a beaker and the mixture was ultrasonicated for 20 minutes and marked as dispersion A. (3) The homogeneous solution of $NiCuZnFe_2O_4$ was added to dispersion A and stirred vigorously. (4) Once thoroughly mixed, 2 M NaOH was added to the mixture dropwise to increase its pH to 11. NaOH converts salt solutions into their respective hydroxide precipitates. (5) The precipitates were heated at 60 °C for 2 h with continuous stirring. (6) The precipitates were vacuum filtered and washed with warm water several times to eliminate nitrate impurities. (7) The precipitates were oven dried for 24 h and calcined at 300 °C for 2 h. As synthesized black coloured FCOB adsorbent was oven dried overnight and further utilized in the adsorption study of CV dye. The schematic diagram for synthesis of FCOB is shown in Fig. 1.

2.3. Characterizations

The Field Emission-Scanning Electron Microscopy (FE-SEM) technique was used to evaluate the topology, surface morphology, and shape/texture of BTBC, FCOB, and FC-CV (FCOB adsorbent after CV adsorption). It was conducted using a NanoSEM 450 FE-SEM FEI Nova instrument. Quantitative and qualitative elemental analysis (Energy Dispersive Spectroscopy-EDS) of FCOB and FC-CV were performed using an EDS detector alongside SEM analysis. The surface roughness quantification of BC300, BTBC, FCOB, and FC-CV was done using the high-resolution Atomic Force Microscopy (AFM) method (Dimension Icon AFM, Bruker, Germany). Thin films were used instead of rough solid samples in tapping mode AFM analysis to minimize the risk of tip damage, as the sharp tip intermittently taps the sample surface. The structural functional groups of LP, BC300, BTBC, FCOB, and FC-CV were confirmed using FT-IR analysis (PerkinElmer IR spectrometer, KBr pellet as

a reference, transmittance mode, 400–4000 cm^{-1}; 1 mg sample + 200 mg). The thermal analyses of BC300, BTBC and FCOB (*e.g.*: TGA) were conducted using SDT Q600 V20.9 Build 20 Thermal Gravimetric analyzer at three different heating rates of 5 °C min^{-1}.

Dynamic Light Scattering (DLS) method (HORIBA SZ-100Z particle size analyzer) was employed to determine the particle size of BTBC and FCOB, as well as the zeta potential of FCOB. The samples (0.01 wt%) were sonicated for 10 min in distilled water, and the suspension pH was adjusted to 2–10 using 0.1 M HCl/NaOH. The UV-Visible spectroscopy (TCC-240A UV-Vis spectrophotometer, Shimadzu; 200–800 nm) was used to measure the concentration of adsorbate dye CV throughout all the experiments.

2.4. Adsorption and recycling studies of FCOB

Aqueous stock solution of CV was prepared with concentration of 600 mg L^{-1}. The adsorption experiment of CV by FCOB was performed at different pHs (2 to 8), adsorbent doses (10 to 90 mg), adsorbate concentrations (15 to 600 mg L^{-1}), and contact times (10 to 190 min). Adsorption experiments were carried out at four different temperatures (30, 40, 50, 60 °C). Temperatures of 30–60 °C were selected to represent a practical range for adsorption studies without exceeding the thermal stability of the adsorbent. The concentrations of CV dye solutions before and after adsorption were determined from the calibration curve (Fig. S2). The absorbance of CV was measured at λ_{max} = 590 nm using UV-Vis analysis. The removal percentage (R%) and adsorption capacity at equilibrium (q_e in mg g^{-1}) were measured using eqn (1) and (2), respectively.

$$R\% = \frac{(C_0 - C_e)}{C_0} \times 100\% \quad (1)$$

$$q_e = \frac{(C_0 - C_e) \times V}{m} \quad (2)$$

where, C_0 and C_e represent initial and final CV dye concentrations in unit mg L^{-1}. V and m are volume of CV dye solution in L and adsorbent dosage in g respectively. The volume of CV dye solution was kept constant at 0.04 L throughout the experiment.

100 mL conical flask was used throughout the adsorption experiment. The CV dye + FCOB mixture was stirred on magnetic stirrer until the equilibrium was achieved during each adsorption parameter experiment. FCOB was removed from CV solution using a centrifuge machine at the end of adsorption.

Adsorption isotherms offer insights into the adsorption mechanism, indicating whether the process is physical or chemical, as well as the types of interactions between CV and the FCOB adsorbent. To determine the isotherm parameters for CV adsorption on FCOB, several non-linear models—including Langmuir (eqn (3)), Freundlich (eqn (4)), Liu (eqn (6)), Temkin (eqn (5)), and Dubinin–Radushkevich (eqn (7))—were applied. Additionally, the separation factor (R_L), Polanyi potential (ε), and adsorption energy (E) were calculated using eqn (8)–(10), respectively.

$$q_e = \frac{q_m K_L C_e}{1 + K_L C_e} \quad (3)$$

$$q_e = K_F C_e^{\frac{1}{n_F}} \quad (4)$$

$$q_e = B \ln(A_T C_e) \quad (5)$$

$$q_e = \frac{q_m K_g C_e{}^n L}{1 + K_g C_e{}^n L} \quad (6)$$

$$q_e = q_m \exp(-\beta \varepsilon^2) \quad (7)$$

$$R_L = \frac{1}{1 + K_L C_0} \quad (8)$$

$$\varepsilon = RT \ln\left(\frac{C_s}{C_e}\right) \quad (9)$$

$$E = \frac{1}{\sqrt{2\delta}} \quad (10)$$

In this study, the symbols R, T, q_m, K_L, K_f, n, b_T, A_T, δ, and C_s represent the universal gas constant (8.314 J mol^{-1} K^{-1}), adsorption temperature, Langmuir maximum adsorption capacity (mg g^{-1}), Langmuir constant (L mg^{-1}), Freundlich constant (mg g^{-1}) (L $mg^{-1})^{1/n}$, heterogeneity factor, Temkin constant (J mol^{-1}), Temkin equilibrium binding constant (L g^{-1}), the constant related to adsorption energy (mol^2 kJ^{-2}) (eqn (10)), and the saturation concentration of CV (mg L^{-1}), respectively. The value of b_T was determined using the relation $B_1 = RT/b_T$.

The kinetics of CV adsorption on FCOB were evaluated using four non linear form of models: pseudo-second-order (eqn (11)), pseudo-first-order (eqn (12)), Elovich (eqn (13)), and intraparticle diffusion (eqn (14)). The model that best fitted the experimental data was identified to elucidate the adsorption kinetics of CV on FCOB.

$$q_t = q_{e1}[1 - e^{-k_1 t}] \quad (11)$$

$$q_t = \frac{q_{e2}{}^2 k_2 t}{k_2 q_{e2} t + 1} \quad (12)$$

$$q_t = \frac{1}{\beta} \ln(1 + \alpha\beta t) \quad (13)$$

$$q_t = k_p \sqrt{t} + C \quad (14)$$

Here, q_t (mg g^{-1}), k_p (mg g^{-1} $min^{-1/2}$), t (min), k_1 (min^{-1}), k_2 (g mg^{-1} min^{-1}), and a_e (mg g^{-1} min^{-1}) represent the adsorption capacity at time t, the intraparticle diffusion rate constant, time, the pseudo-first-order rate constant, the pseudo-second-order rate constant, and the Elovich constant, respectively. The parameter C (mg g^{-1}) reflects the boundary layer thickness and provides insight into its influence on the adsorption rate.

The nonlinear forms of the adsorption isotherm and kinetic models were used as non-linear fitting avoids potential errors associated with linearization and provides a more accurate representation of the adsorption process.[29]

Furthermore, the influence of temperature was examined to understand the adsorption nature of CV on FCOB. From the slope and intercept of the $\ln k_e$ *versus* $1000/T$ (K^{-1}) plot, the thermodynamic parameters enthalpy change ($\Delta H°$, kJ mol^{-1}) and entropy change ($\Delta S°$, J mol^{-1} K^{-1}) were determined using eqn (15). These values were subsequently applied to calculate the Gibbs free energy change ($\Delta G°$, kJ mol^{-1}) through eqn (16).

$$\Delta G^\circ = \Delta H^\circ - T\Delta S^\circ \quad (15)$$

$$\ln K_e = \Delta S^\circ R - \Delta H^\circ RT \quad (16)$$

where, $K_e = q_e/C_e$.

For regeneration studies, 1 N HCl was used as the desorbing agent. In each cycle, 40 mL of HCl solution was added to 30 mg of dye-loaded adsorbent (FC-CV) at a pH of 2–3. The mixture was stirred at 250 rpm on a magnetic stirrer at a fixed temperature of 30 °C for 30 minutes. After desorption, the FCOB was filtered, washed thoroughly with distilled water, dried, and reused for the adsorption of CV dye under the same optimized conditions. Thus, FCOB adsorbent was regenerated and reused for five cycles to assess its performance.

2.5. Artificial neural network (ANN)

ANN is a machine learning process inspired by complex structure and functioning of human brain.[30] It is a kind of artificial intelligence that seeks to replicate the neural framework of human brain, enabling processors to analyse brain signals and make conclusions analogous to human brain in computational systems.[31] They recognize links and patterns in the data enabling the tasks like decision making, classification and prediction. This ability enables ANN to express complex non-linear functions given the right activation functions, number of neurones, and training procedure. Its framework comprises of input layer, one or more hidden layers, and output layer. *Via* weighted linkages, input layer neurons receive the data and passes to the 1st hidden layer neurons. A neuron performs its function in the hidden layer and passes its output to the next hidden layer. The number of hidden layers varies depending on the complexity of the architecture.[32] The activated inputs from the last hidden layer pass to output layer and convert them to the desired outputs.[33] During the network training procedure, a method called trial-and-error was used over many epochs (trials) to get the best results, with the goal of increasing R^2 and decreasing root-mean-square error (RMSE). The ANN framework of the present study is given in Fig. 2. The framework consists of total 5 inputs (*i.e.* pH, FCOB mass, CV dye concentration, temperature, and time),8 hidden layers for R% output and hidden layers for q_e output, and 2 output layer (*i.e.*, R%, q_e). The experimental data acts as cornerstone, enabling the ANN model to learn the complicated relationships between inputs and outputs. ANN rapidly predicts the results for another new inputs after training on datasets. This allows the fast forecasting of predicted results under specific experimental scenarios. Interestingly, the dataset comprising of experimental dataset is split into 70% for training, 15% for validation, and 15% for testing. This partition assures effective learning,

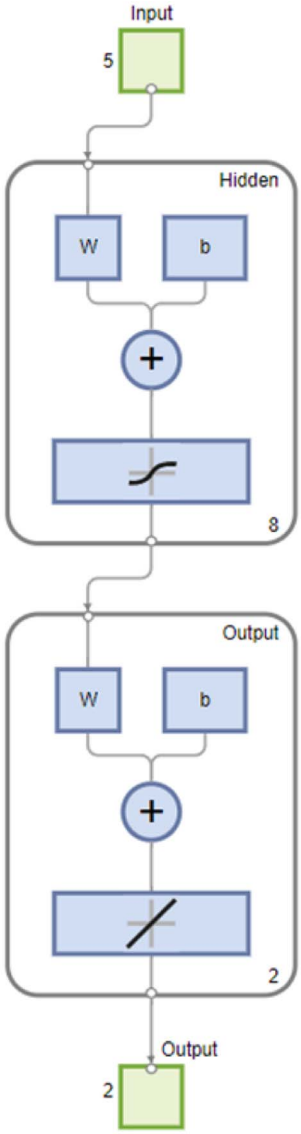

Fig. 2 ANN architecture.

verifies precision and improves ANN's capability for generalizing predictive power.

All the adsorption experiment datasets were trained utilising an Artificial Neural Network (ANN) method using MATLAB (R2022b) programming platform. Neural Network Model (nftool) is a graphical interface (GUI) in MATLAB, which was used to build, train and assess feed-forward neural networks for model fitting and regression analysis. The research dataset was optimised and trained to attain a minimum mean square error (MSE) (eqn (17)) and an R-value (eqn (18)) around one.

$$\mathrm{MSE} = \frac{1}{N}\sum_{i=1}^{N}\left(\left|y_{\mathrm{pred},i} - y_{\mathrm{exp},i}\right|\right)^2 \quad (17)$$

$$R^2 = 1 - \frac{\sum_{i=1}^{N}\left(\left|y_{\mathrm{pred},i} - y_{\mathrm{exp},i}\right|\right)^2}{\sum_{i=1}^{N}\left(\left|y_{\mathrm{pred},i} - y_{\mathrm{m}}\right|\right)^2} \quad (18)$$

where N = number of collected data points, $y_{\mathrm{pred},i}$ = predicted output value, $y_{\mathrm{exp},i}$ = experimental output value, y_{m} = mean value of experimental outputs, i = indexes experimental data points.

3. Results and discussion

3.1. SEM-EDX

Fig. 3a and b represent SEM images of BTBC and FCOB. Seemingly, BTBC has sponge-like structure possessing high porosity. The rough porous framework observed in SEM image of BTBC is an indicative of the liberation of volatile gases during pyrolysis and successful alkaline activation by NaOH. It is not smooth but has an intricate network of small voids and cavities.[34] While, FCOB has compact, dense, layered and folded structure. It has less visible pores than BTBC. It has less number of cavities than BTBC, rather it has some large cavities. Most of the small voids of BTBC are blocked due to $NiCuZnFe_2O_4$ deposition.

SEM image of FC-CV is shown in Fig. 3c. After adsorption of CV dye, FCOB adsorbent particles become agglomerated. The surface displays pore obstruction along with limiting surface roughness. It appears swollen and smoother in comparison to the pristine FCOB, signifying effective surface coverage and interaction between CV and active functional sites of FCOB.

It is worth noting that SEM analysis was performed only for the BTBC, FCOB, and FC-CV. SEM analysis of BC300 could provide further insight to clarify the changes in the morphology of biochar before and after alkali modification, and will be considered in future work.

The elemental composition of adsorbent FCOB (before adsorption) and FC-CV (after CV adsorption) determined through EDS analysis is shown in Table 1. Their EDS spectra are shown in supplementary file (Fig. S3). The presence of Fe (2.32%), Ni (0.43%), Cu (0.60%), and Zn (0.44%) verifies the successful synthesis of ferrite spinel composite of biochar (FCOB). The presence of Na, Mg, Al, Si, P, and Ca in FCOB is attributed to halophytic nature of *Suaeda monoica* allowing it to absorb and accumulate these elements from soil. C content of FCOB is the highest followed by O and N. Following adsorption, in FC-CV, the total C content rises as due to the deposition of carbon-rich CV molecule on FCOB. The decline in O content indicates that O-rich functional groups of FCOB react with CV during adsorption.[35] Generally, N content should increase after CV adsorption, but this is not a case here. It may be due to the surface obscuring by CV dye layer, relative dilution by enhanced carbon and metal signals, potential ion transfer or leaching,

Table 1 EDS elemental composition (%wt) before (FCOB) and after (FC-CV) CV adsorption

	Percentage (%)	
Elements	FCOB (before adsorption)	FC-CV (after adsorption)
C	59.50%	75.2%
N	10.96%	—
O	23.98%	23.2%
Na	0.27%	1.1%
Mg	0.46%	1.1%
Al	0.06%	—
Si	0.07%	—
P	0.14%	—
Ca	0.77%	0.8%
Fe	2.32%	13.5%
Ni	0.43%	2.8%
Cu	0.60%	4.1%
Zn	0.44%	3.1%

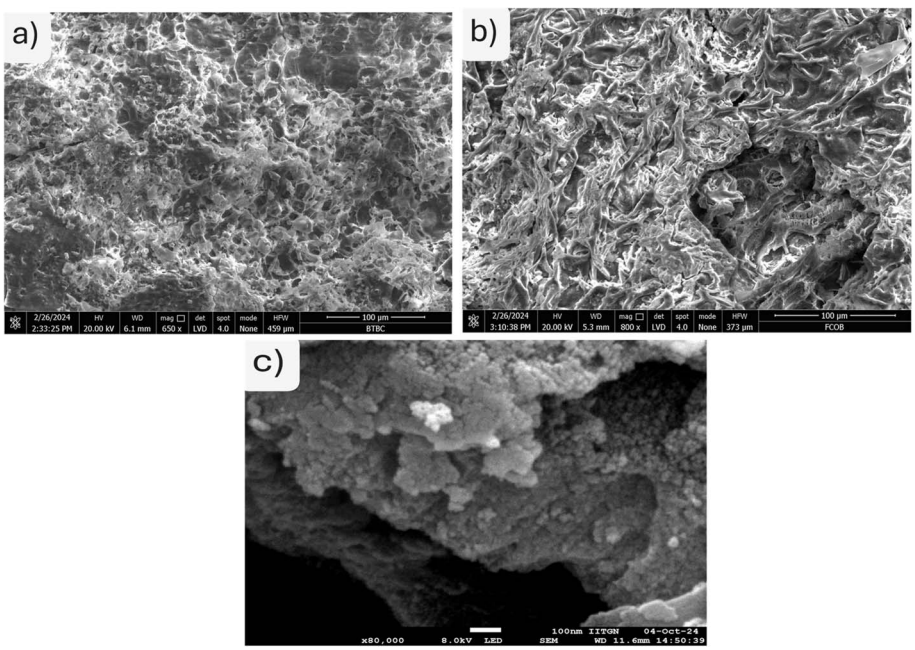

Fig. 3 SEM images of (a) BTBC, (b) FCOB, and (c) FC-CV.

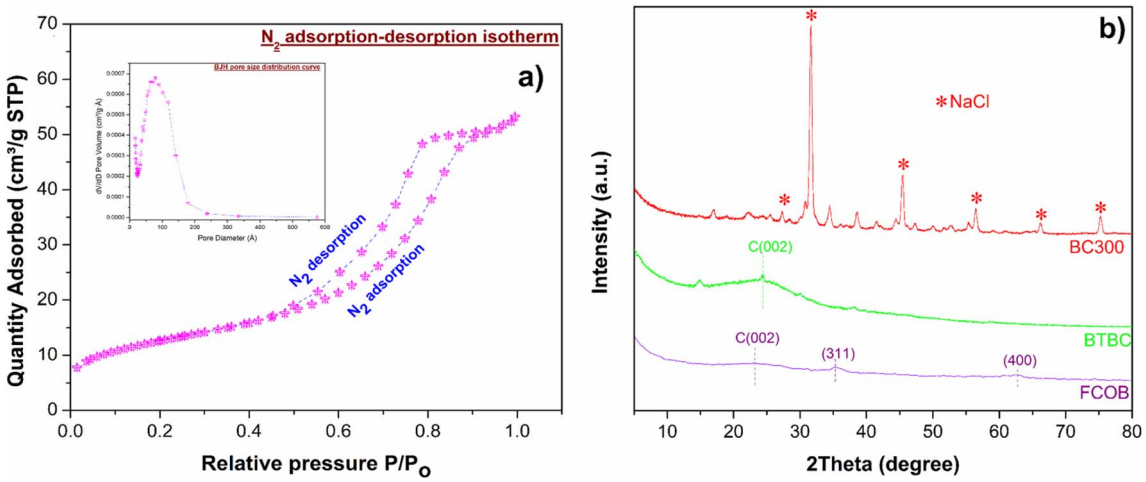

Fig. 4 (a) BET, (b) XRD plots of FCOB.

and limits in EDS sensitivity for light or buried elements. CV, a cationic dye, can form stable complexes with Fe, Cu, Ni, and Zn *via* nitrogen lone pairs, so their content would be expected to remain nearly the same after adsorption. The apparent increase is attributed to the low sensitivity and inherent limitations of EDS, moreover, it is not an absolute technique for compositional analysis but a surface-sensitive and semi-quantitative method that provides only approximate elemental information.[36] A similar phenomenon was observed for the increase in Ca, Mg, and Na, where CV dye likely displaced these cations through ion exchange; although their content would be expected to decrease, the EDS signal appeared higher.

3.2. BET

The Brunauer–Emmett–Teller (BET) analysis measures the specific surface area through N_2 gas adsorption, which is crucial for comprehending the adsorption performance and efficiency of porous materials in various applications. It also gives significant insight into other surface features (*e.g.*: pore size distribution, pore size, pore volume, hysteresis loop, and isotherm type) of porous materials. N_2 adsorption–desorption isotherm and BJH pore size distribution curve of FCOB is shown in Fig. 4. FCOB composite demonstrates BET surface area, pore volume, and pore size of 44.64 $m^2\ g^{-1}$, 0.078 $m^3\ g^{-1}$ and 7.0 nm respectively. FCOB exhibits moderate to low N_2 adsorption ($\approx$7 to 53 $cm^3\ g^{-1}$) within 0 to 1 range of P/P_0. FCOB displays isotherm type IV(a), characteristic of mesoporous materials, as confirmed by its pore size which is between 2 to 50 nm.[37] In type IV(a) isotherm, hysteresis develops accompanied by capillary condensation. It occurs when pore width exceeds a certain width that is affected by temperature and adsorption system. The hysteresis loop corresponds to H3 hysteresis type. In H3 type, as the relative pressure increases, the gradients of the adsorption and desorption curves slowly increase, which suggests a narrow hysteresis loop and a quickly growing adsorption volume. Adsorption saturation is not reached when the equilibrium pressure is near to saturated vapour pressure, which often signifies that pore shape is grooved by flaky particles or wedged with opening at both sides. The slit shaped pores probably contribute significantly to the facilitation of CV dye adsorption *via* providing expanded and easily accessed FCOB surface for interaction.

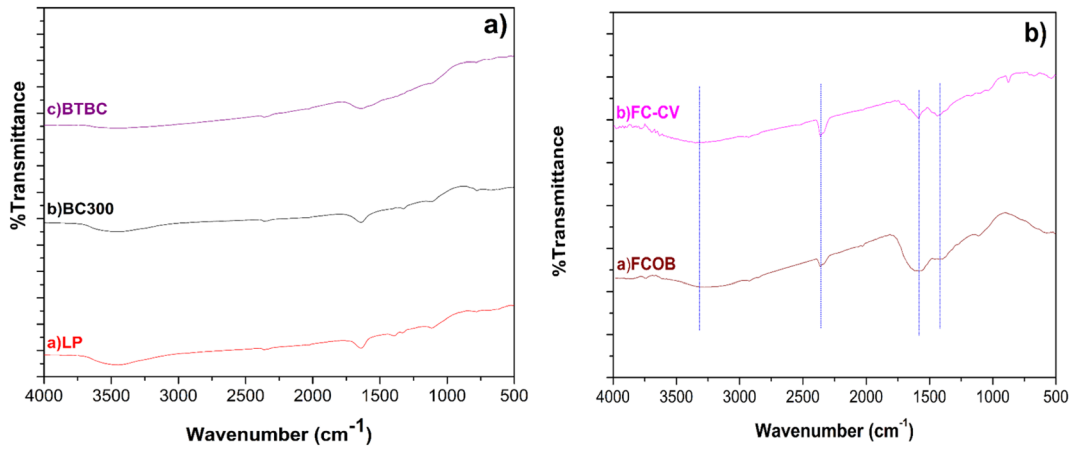

Fig. 5 FT-IR graph of (a) LP, BC300, BTBC; and (b) FCOB, FC-CV.

It is worth noting that BET analysis was performed only for the final adsorbent (FCOB). Characterization of the precursor materials (BC300, BTBC, FC-CV) could provide further insight into the structural development and will be considered in future work.

3.3. p-XRD

Powder X-ray diffraction, or p-XRD, is a potent method for determining the crystalline structure or arrangement, phase composition, crystalline size, and crystallinity. Stacked p-XRD patterns of BC300, BTBC, and FCOB is shown in Fig. 4. The dominance of NaCl peaks in BC300 is attributed to the halophytic nature of *Suaeda monoica*, therefore, it accumulates lots of salts, especially NaCl.[38] Weili Jiang *et al.* reported the similar result in XRD pattern of other species of *Suaeda monoica* (*e.g.*: *Suaeda salsa*), indicating the inherent salt-accumulating nature of halophytic plants.[39] There are six peaks in XRD pattern of BC at 27.3°, 31.6°, 45.5°, 56.5°, 66.2°, and 75.2° corresponding to (1 1 1), (2 0 0), (2 2 0), (2 2 2), (4 0 0) and (4 2 0) crystal planes of NaCl.[40] The lack of broad peaks in BC300 is attributed to dominance of crystalline salts (*e.g.*: NaCl), which may obscure the signals of amorphous carbon. After the base treatment, NaCl crystal peaks vanish in BTBC, reflecting the removal of NaCl. BTBC has aromatic layers of amorphous carbon stacked, which is supported by the wide peak between 15° and 30°.[41] It is indexed as C(0 0 2). This confirms effective activation of BC300 by NaOH, leading to increased porosity and amorphous nature. The C(0 0 2) peak shifted slightly from ≈24° to 23° in FCOB, indicating increased interlayer spacing due to structural modification by $NiCuZnFe_2O_4$ particles. The XRD pattern of FCOB clearly shows the two most intense characteristic peaks of ferrite spinel $NiCuZnFe_2O_4$ approximately at $2\theta \approx 35.5°$ and 62.9°, corresponding to (3 1 1) and (4 4 0) crystal planes, respectively.[42] This further demonstrates that $NiCuZnFe_2O_4$ was successfully incorporated onto BTBC to yield FCOB. Since FCOB has a mole ratio of BTBC : $NiCuZnFe_2O_4$ 2 : 1, the absence of additional distinctive peaks of $NiCuZnFe_2O_4$ in FCOB may be explained by its low concentration in comparison to BTBC.

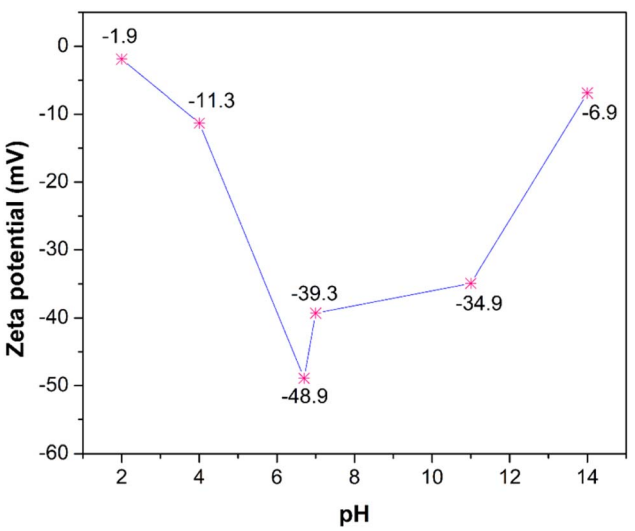

Fig. 6 Zeta potential plot of FCOB.

3.4. FT-IR

The FTIR spectra of LP, BC300, and BTBC are presented in Fig. 5a, while those of FCOB and FC-CV are shown in Fig. 5b. LP shows a broad peak at 3455 cm^{-1} corresponding to O–H stretching vibrations, indicative of hydrogen-bonded groups such as alcohols, phenols, or bound water. The peak at 2346 cm^{-1} is attributed to atmospheric CO_2 interference, while in BC300 it may also arise from residual CO_2 generated during pyrolysis. The peak at 1641 cm^{-1} is associated with amide, C=O stretching, N–H bending, or aromatic C=C stretching, indicating the presence of proteins and/or aromatic compounds. The peak at 1334 cm^{-1} can be assigned to O–H bending vibrations of carbohydrates. The peak at 1396 cm^{-1} corresponds to COO^- symmetric stretching from carboxylate groups, reflecting fatty acids or amino acids. Peaks at 1110 cm^{-1} (C–O, C–N stretching) and 780 cm^{-1} (C–N stretching, =C–H bending) are related to cell wall components such as cellulose, hemicellulose, pectin, lignin, and proteins.[43] The absence of the 1396 cm^{-1} peak in BC300 and BTBC is due to pyrolytic decomposition or base-induced conversion of carboxyl groups. Overall, most functional groups present in LP are preserved in BC300 and BTBC, consistent with low-temperature biochar preparation. FTIR spectra of FCOB showed a broad O–H stretching band at 3277 cm^{-1}, shifted from 3455 cm^{-1} in LP/BC300/BTBC, indicating hydrogen bonding and interaction with ferrite metal ions. The band at 1594 cm^{-1} (C=O/N–H/C=C) also shifted to higher wavenumber confirming biochar–ferrite coordination.[44] Peaks at 1400 cm^{-1} (COO^-) and 1106 cm^{-1} (C–O/C–N/O–H) further supported composite formation. These shifts collectively may verify the successful incorporation of ferrite spinel onto biochar.

The FTIR spectrum of FCOB shows a broad O–H stretching band at 3370 cm^{-1}, which shifted slightly to 3277 cm^{-1} after CV adsorption, suggesting hydrogen bonding interactions.[45] The C=O/C=C/N–H vibration band at 1594 cm^{-1} in FCOB shifted to 1587 cm^{-1}, indicating electrostatic interactions and π–π stacking between CV molecules and the biochar–ferrite surface. The symmetric stretching vibration of the COO^- group appeared at 1400 cm^{-1} in FCOB and shifted to 1421 cm^{-1} after adsorption, while the C–O/C–N stretching band at 1100 cm^{-1} shifted slightly to 1106 cm^{-1}, reflecting the participation of surface functional groups in dye binding. Importantly, new peaks appear at 873 and 685 cm^{-1} in the FC-CV spectrum, corresponding to aromatic = C–H bending and skeletal vibrations, which are characteristic of CV.[46] The emergence of these peaks, absent in pristine FCOB, provides direct evidence for the successful adsorption of CV molecules onto the composite surface. These spectral changes collectively demonstrate that CV adsorption onto FCOB occurs mainly through hydrogen bonding, electrostatic attraction, π–π interactions, and surface complexation mechanisms.

3.5. Surface charge measurement and particle size analysis

The extent of electrostatic repulsion or attraction between particles is measured by zeta potential (ζ), which refers to the electrical potential at the slipping plane of a particle suspended in a liquid.[47] Thus, zeta potential analysis was utilised to

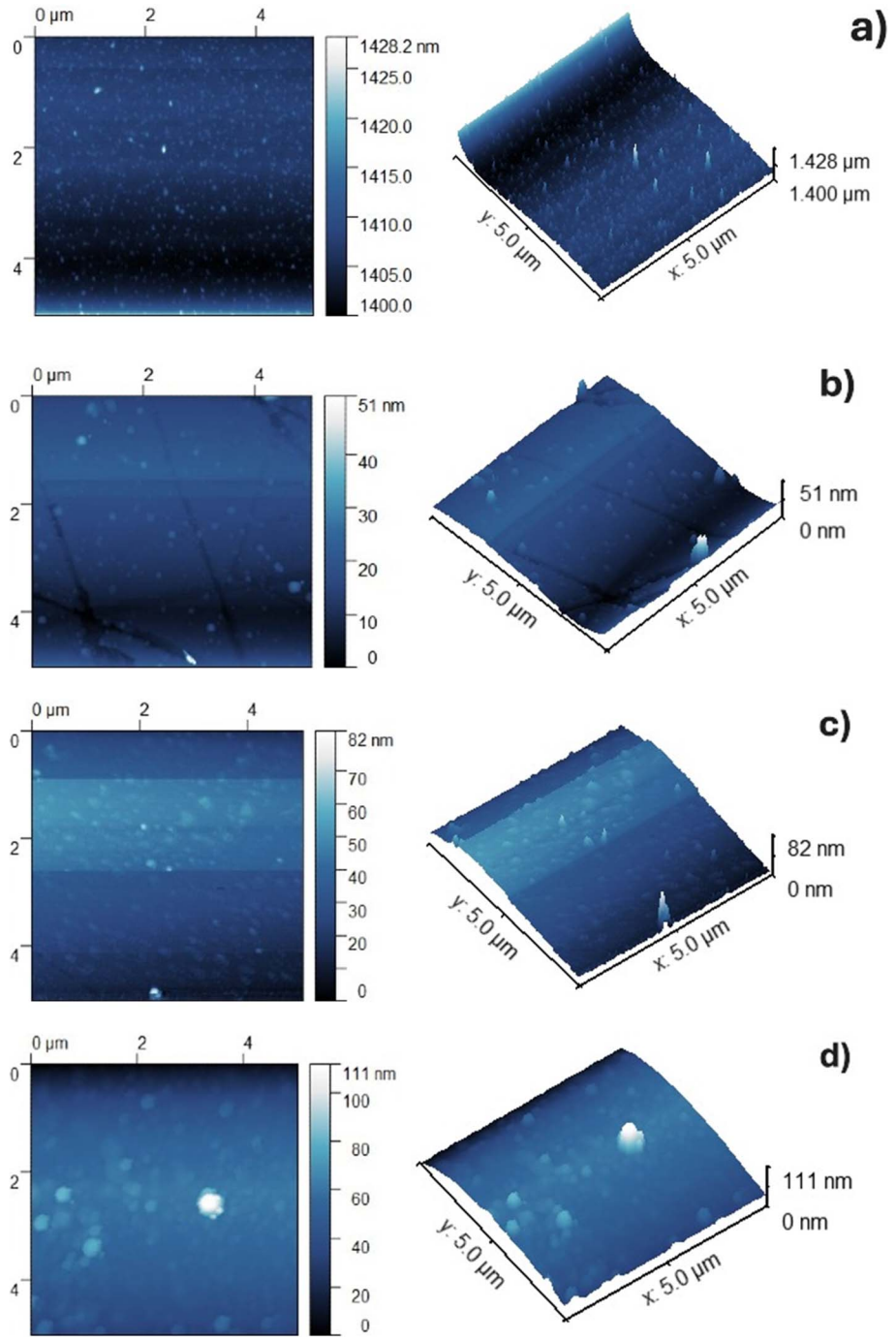

Fig. 7 2D and 3D AFM images of (a) BC300, (b) BTBC, (c) FCOB, and (d) FC-CV

characterise surface charges of FCOB at different pHs. Isoelectronic point or point zero charge (pH_{pzc}) is the pH value at which ζ value is zero.[48] It means that net surface charge of materials is zero at pH_{pzc}. It affects the adsorption process under certain pH ranges.[48] The plot of zeta (ζ) potential values *vs.* pH for FCOB is given in Fig. 6. FCOB exhibited −ve zeta potential values across all acidic and alkaline pHs, suggesting a consistently −vely charged surface under all experimental conditions. The −ve zeta potential of FCOB across all pHs is ascribed to the abundance of O-containing functional groups, such as, COO^-, –OH, C═O, *etc.* on its surface sites. Similar results have been reported by Samsuri A. W., reporting biochar adsorbent with a −ve zeta potential over whole pH range due to O-functionalized groups.[49]

The particle sizes measured using DLS (Dynamic Light Scattering) method are 7.4 and 9.3 µm for BTBC and FCOB respectively. The deposition of $NiCuZnFe_2O_4$ onto BTBC leads to denser and larger particle dimensions, hence, particle size of FCOB is greater than that of BTBC.

Table 2 Roughness parameters

Material	S_a (nm)	S_q (nm)	S_{sk}
BC300	2.4	3.1	0.86
BTBC	4.5	5.4	−0.14
FCOB	10.3	12.1	−0.001
FC-CV	10.4	13.7	−0.64

3.6. AFM

The surface topography and nanoscale roughness of all the components were examined using AFM analysis. 2D and 3D AFM image of BC300, BTBC, FCOB and FC-CV are shown in Fig. 7a–d. 3D images suggest the presence of unevenly shaped particles with different heights, which supports the heterogeneous nature of all biochar components. The investigation of surface roughness parameters was done using Gwyddion (64 bit) software. The mean roughness (S_a), RMS roughness (S_q), and skew (S_{sk}) for all the components are given in the Table 2. It is clear that mean roughness (S_a) value of BC300 (2.4 nm) increases after its base activation (4.5 nm) and which is further increased to 10.3 nm upon ferrite spinel incorporation in FCOB. After CV adsorption, S_a and S_q value increases indicating surface changes of adsorbent due to CV dye interaction.

3.7. TGA

Thermal analysis of adsorbents is essential for understanding their thermal stability, structural integrity, and adsorption performance under varying temperatures. Thermal analysis identifies the temperatures at which the adsorbent begins to decompose or lose mass. It ensures that the adsorbent can withstand operational temperatures in industrial processes without degradation. Thermogravimetric Analysis (TGA) gives information about thermal stability and decomposition behaviour by measuring the mass loss of a material as a function of temperature or time. The TGA curves of BC300, BTBC, and FCOB are shown in Fig. 8.

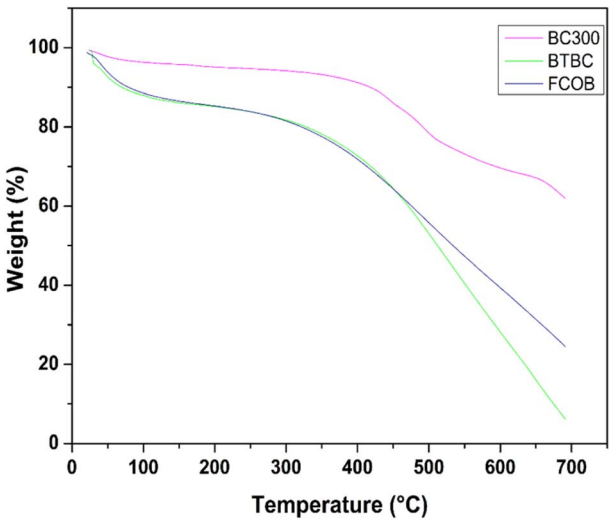

Fig. 8 TGA graph of BC300, BTBC, and FCOB.

The TGA curves of BC300, BTBC, and FCOB reveal a broadly similar three-stage decomposition profile. The initial stage, occurring below ~150 °C, is dominated by the evaporation of physically adsorbed water.[50] In the first stage (21–150 °C), both BTBC and FCOB display a similar decomposition pattern, as also evident from the overlapping nature of their TGA curves (Fig. 8). Nevertheless, a slight quantitative difference is observed, as BTBC shows 13.38% weight loss, whereas FCOB shows 12.21%. This marginally lower mass loss in FCOB may be explained by the incorporation of ferrite particles, which can partially block pores and reduce the amount of water retained through capillary forces and hence lower the moisture loss. The second stage (≈151–400 °C) corresponds to the breakdown of more labile components, including residual hemicellulose, cellulose, bioactive compounds (like resins, tannins, cardiac glycosides, terpenoids, flavonoids, phenols, acidic compounds, and glycosides, lignin) and oxygen-containing groups.[51–56] At higher temperatures (401–691 °C), the third stage is mainly attributed to degradation of residual lignin and progressive oxidation of fixed carbon, which leads to the evolution of gaseous products such as CO and CO_2.[52,57,58]

Although the overall decomposition pattern is common to all three samples, the extent of mass loss and the underlying mechanisms differ markedly. BC300 exhibits relatively low weight losses in both the first (4.08%) and second (4.10%) stages, consistent with the fact that most of its hemicellulose and volatile compounds had already been decomposed during pyrolysis at 300 °C, leaving behind a carbon-rich framework.[59] In contrast, BTBC undergoes pronounced weight losses in the first (13.38%) and second (13.38%) stages, attributable to the alkaline treatment, which introduces abundant hydrophilic functional groups (–OH, –C═O, –COOH, –OC = O). These groups enhance moisture retention and increase the thermal lability of the carbon matrix.[60] So it makes it more prone to decomposition and leading to a remarkably high loss of 66.43% in the third stage, where lignin, salts, and oxygenated functionalities also decompose. For FCOB, as mentioned earlier, its initial weight loss (12.21%) is slightly lower than that of BTBC due to partial pore blocking by ferrite spinel particles; the subsequent stages (14.68% and 47.24%) remain substantial. This is because ferrite spinels catalyze the decomposition of residual functional groups and accelerate oxidation of the carbon framework, while remaining thermally stable themselves.[61] During thermal treatment, inherently present mineral constituents in *Suaeda monoica* leaves (Mg, Al, Si, P, and Ca), occurring in both inorganic forms (*e.g.*, salts, oxides, phosphates, carbonates) and organically bound forms (*e.g.*, chelates, organometallic complexes, covalently associated with the matrix), interact with the carbon framework of all samples.[62] In BC300, these minerals primarily contribute to structural stability, thereby restricting mass loss across decomposition stages, whereas in BTBC and FCOB, they act more catalytically, accelerating degradation and oxidation in the higher temperature range (401–691 °C) and amplifying the overall weight loss.

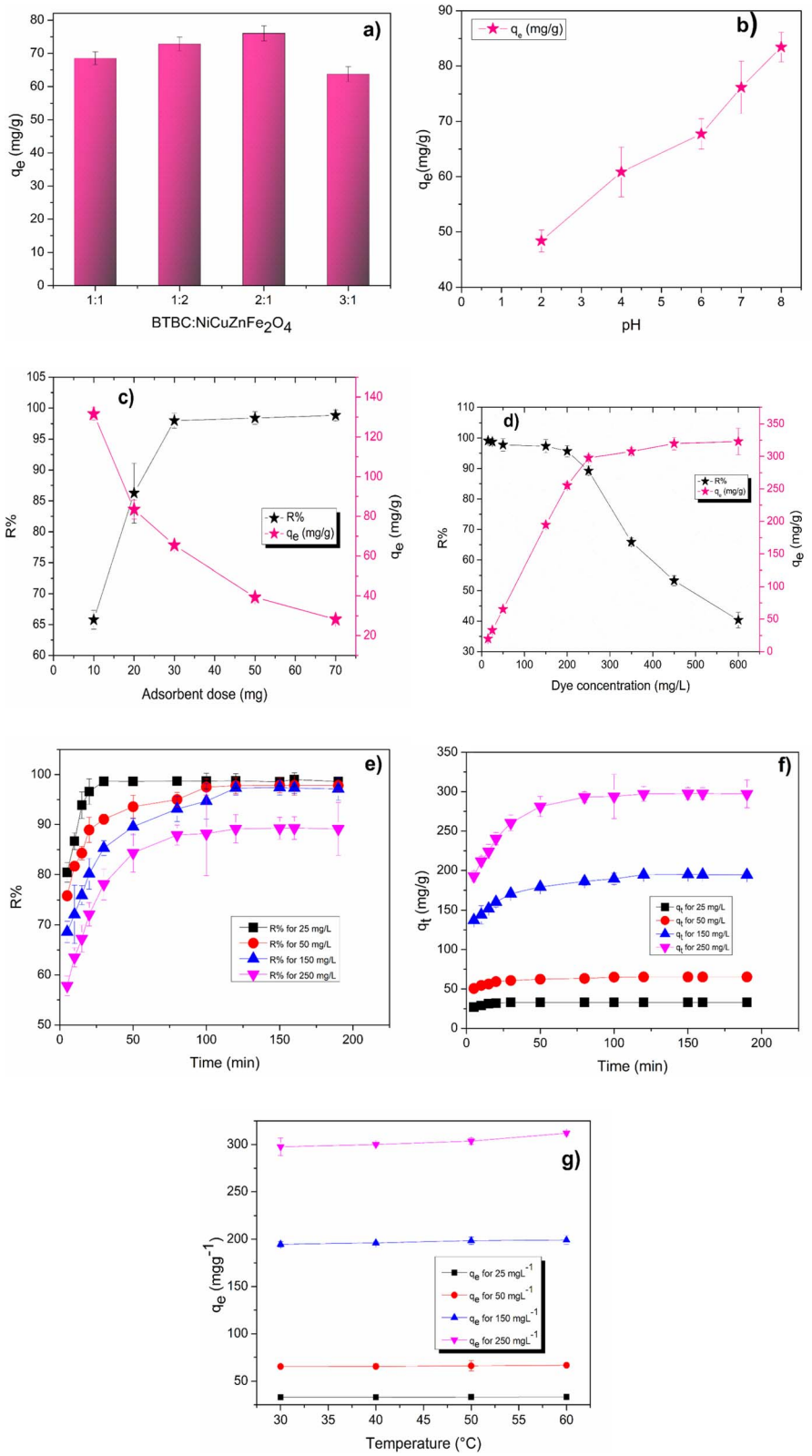

Fig. 9 Effect of different parameters on the adsorption of CV by FCOB: (a) BTBC : NiCuZnFe$_2$O$_4$ content, (b) pH, (c) adsorbent dose, (d) initial dye concentration, (e–f) contact time, and (g) temperature.

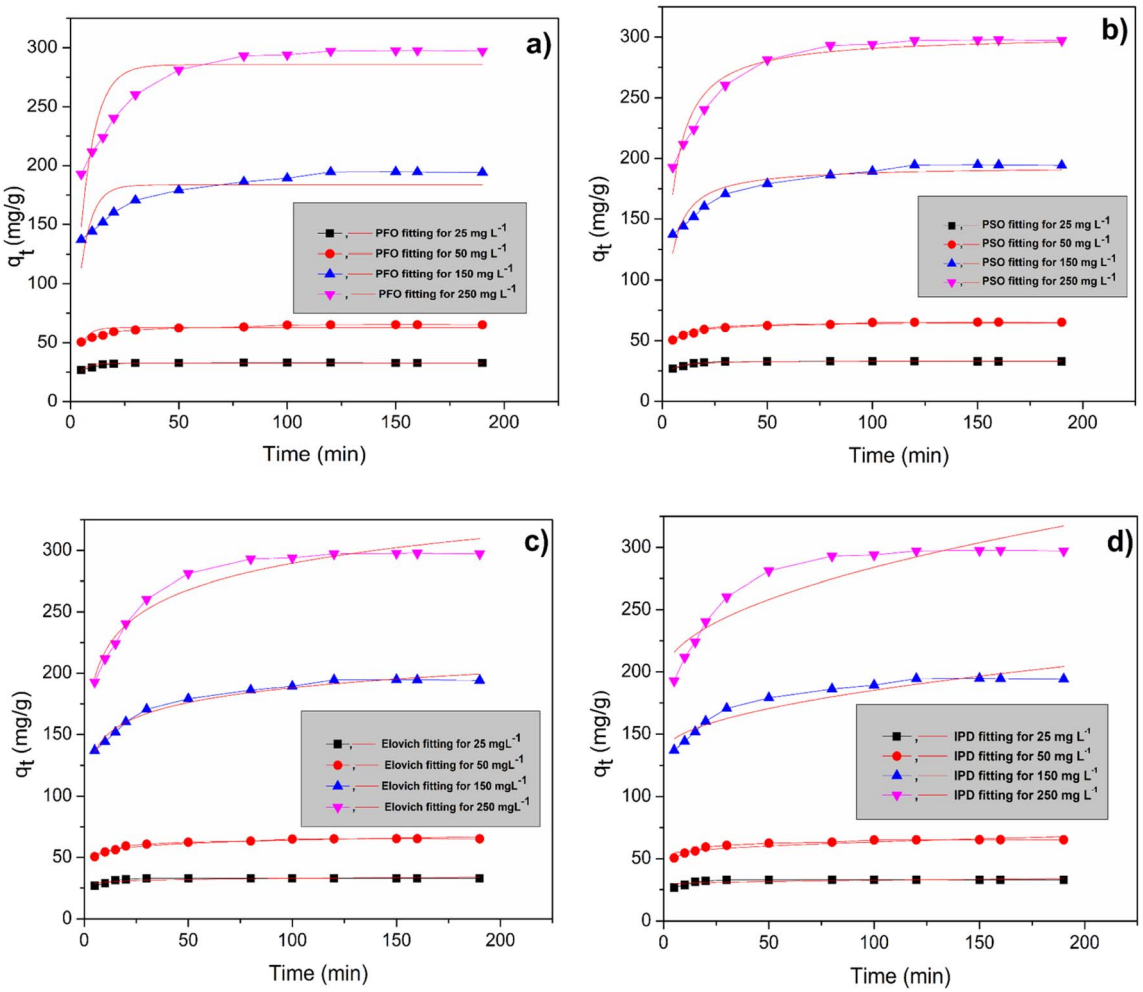

Fig. 10 Non-linear kinetic fitting of CV adsorption onto FCOB: (a) PFO, (b) PSO, (c) Elovich, and (d) IPD at 25–250 mg L^{-1} initial concentrations.

3.8. Effect of different experimental conditions on CV adsorption

3.8.1. Effect of BTBC and $NiCuZnFe_2O_4$ content. As shown in the synthesis section, four FCOB composites were prepared with BTBC : $NiCuZnFe_2O_4$ ratios of 1 : 1, 2 : 1, 1 : 2, and 3 : 1. Among these, the 2 : 1 composite exhibited the highest CV removal capacity (q_e = 86.12 mg g^{-1}), while the 3 : 1 composite showed the lowest (q_e = 75.09 mg g^{-1}) (Fig. 9a). The other conditions were C_0 = 50 mg L^{-1}, m = 0.02 g, t = 190 min, T = 30 °C. The improvement from 1 : 1 to 1 : 2 can be attributed to the higher ferrite content, which enhances surface functionality and promotes dye adsorption. Interestingly, the 2 : 1 composite outperformed 1 : 2, indicating that this ratio achieves the most effective synergistic interaction between BTBC and ferrite, providing optimum surface area and active sites. In contrast, excess BTBC in the 3 : 1 composite likely caused particle agglomeration and dilution of ferrite activity, reducing adsorption efficiency. Therefore, the 2 : 1 composition was selected for further adsorption experiments of CV.

3.8.2. Effect of pH of dye solution. The adsorption of Crystal Violet (CV) onto FCOB was studied across pH 2–8 (Fig. 9b), under constant conditions (m = 0.02 g, t = 190 min, T = 30 °C, V = 0.04 L, C_0 = 50 mg L^{-1}). Given the pK_a of CV (8.64), the dye exists predominantly in its cationic form within this pH range.[63] At acidic pH, the FCOB surface exhibits low negative zeta potential (−1.2 to −3.4 mV), resulting in weak electrostatic attraction. Moreover, the high concentration of H^+ ions at low pH competes with cationic CV molecules for adsorption sites, and the protonated adsorbent surface can repel CV molecules, leading to reduced adsorption.[64] In contrast, at pH 6–8, the zeta potential is highly negative (−48.24 to −34.58 mV), leading to stronger electrostatic interactions with the cationic CV molecules, which favors adsorption. Although the zeta potential at pH 7 is slightly more negative than the surrounding points, this minor deviation does not significantly affect the adsorption behavior. The overall increase in negative surface charge from acidic to alkaline conditions, combined with π–π interactions, hydrogen bonding, surface complexation (as evidenced from FT-IR of FC-CV), and pore filling (as evidenced from BET) between CV and surface functional groups, contributes to the maximum CV adsorption at pH 8.

3.8.3. Effect of adsorbent dose and initial CV concentration. CV dye adsorption was conducted from 10 to 70 mg. Other

Table 3 Kinetic parameters for the adsorption of CV on FCOB

		Initial concentration of CV solution (mg L^{-1})			
Kinetic model	Parameter	25	50	150	250
	$q_{e,exp}$	32.88	64.99	194.61	297.15
PFO	$q_{e,1}$ (mg g^{-1})	32.5 ± 0.28	62.7 ± 1.04	183.6 ± 5.04	285.6 ± 7.79
	k_1 (min^{-1})	0.28 ± 0.02	0.27 ± 0.03	0.19 ± 0.03	0.14 ± 0.02
	R^2	0.79	0.57	0.50	0.66
PSO	$q_{e,2}$ (mg g^{-1})	33.0 ± 0.18	65.2 ± 0.50	193.5 ± 3.21	301.7 ± 4.59
	k_2 (g mg^{-1} min^{-1})	0.02 ± 0.002	0.008 ± 0.0008	0.001 ± 0.0002	0.0008 ± 0.0001
	R^2	0.94	0.93	0.87	0.92
Elovich	α (mg g^{-1} min^{-1})	0.04 ± 0.11	0.14 ± 0.56	0.34 ± 0.79	0.44 ± 95
	β (g mg^{-1})	0.73 ± 0.15	0.29 ± 0.01	0.05 ± 0.002	0.03 ± 0.002
	R^2	0.67	0.94	0.97	0.95
IPD	k_p (mg g^{-1} $min^{-0.5}$)	0.34 ± 0.10	1.12 ± 0.16	5.03 ± 0.51	8.79 ± 1.18
	C (mg g^{-1})	29.1 ± 0.95	52.19 ± 1.41	134.98 ± 4.53	196.01 ± 10.41
	R^2	0.45	0.81	0.89	0.83

conditions were pH = 8, t = 190 min, T = 30 °C, V = 0.04 L, C_0 = 50 mg L^{-1}. As seen (Fig. 9c), R% increases from 10 to 30 mg up to 98%. The increased amount makes the interaction between CV and FCOB more favorable because of increased proximity between the CV and adsorbent, allowing various non-bonding interactions between CV and FCOB, thereby, achieving high R%. After 30 mg, R% did not differ much, however, q_e value decreases much, therefore, 30 mg FCOB dose was optimised for further experiments.

The adsorption of CV by FCOB was examined over 15–600 mg L^{-1} (Fig. 9d). Other conditions were pH = 8, t = 190 min, T = 30 °C, V = 0.04 L, m = 0.03 g. At concentrations ≤200 mg L^{-1}, removal efficiency (R%) remained above 95% due to the abundance of active sites relative to dye molecules, enabling effective adsorbate–adsorbent interactions. Similar observations have been reported for CV adsorption using magnetic biochars, where high R% at low concentrations is attributed to site availability.[65] Beyond 200 mg L^{-1}, R% declined with increasing concentration, reflecting site saturation and the persistence of unadsorbed dye molecules in solution.[66] As shown in Fig. 9d, the adsorption capacity (q_e) increases with rising initial CV concentration, which can be attributed to the stronger mass transfer driving force generated by higher concentration gradients.[67]

3.8.4. Effect of time. Fig. 9e and f show the effect of contact time on CV removal (R%) and adsorption capacity (q_t) at different initial concentrations. Other conditions were pH = 8, T = 30 °C, V = 0.04 L, t = 190 min, m = 0.03 g. At lower concentrations (25–50 mg L^{-1}), >90% removal was achieved within 30 min due to abundant active sites on FCOB. At higher concentrations (150, 250 mg L^{-1}), adsorption was slower, with ~43% removal at 30 min, followed by gradual uptake until equilibrium at 120 min. The longer equilibrium time reflects progressive site occupation and competition among dye molecules, leading to surface saturation.[22]

3.8.5. Effect of temperature. The effect of temperature on CV adsorption is shown in Fig. 9g. Other conditions were pH = 8, t = 190 min, m = 0.03 g, V = 0.04 L, C_0 = 50 mg L^{-1}. q_e increased with temperature (30–60 °C), more markedly at higher concentrations; for instance, q_e rose from 194.6 to 199.2 mg g^{-1} at 150 mg L^{-1} and from 297.5 to 312.1 mg g^{-1} at 250 mg L^{-1}, while only slight increases occurred at 25 and 50 mg L^{-1}. This is because low concentrations quickly saturate the available sites, whereas at higher concentrations, elevated temperature enhances diffusion and utilization of additional sites. The rise in q_e with temperature reflects increased kinetic energy and diffusion of CV molecules, along with activation of additional sites on the FCOB surface. This also proves the endothermic nature of the adsorption behavior was also reported by Brichi *et al.* for the adsorption of CV by γ-Fe_2O_3/bentonite magnetic composite is consistent with the spontaneity confirmed by the thermodynamic parameters (Section 3.8.8).[68]

3.8.6. Kinetic investigations. The plot of q_t against t was fitted non-linear approach, using four methods pseudo-first order (PFO), pseudo-second order (PSO), Elovich, and intra-particle diffusion (IPD) model. The non-linear kinetic fitting curves for varying CR concentration are provided in Fig. 10 and results are summarized in Table 3. The adsorption of CV onto FCOB at initial concentrations of 25, 50, 150, and 250 mg L^{-1} was best described by the pseudo-second-order (PSO) kinetic model, indicating that the process is predominantly governed by chemical interactions and occurs *via* chemisorption on the adsorbent surface. The value of $q_{e,1}$ for 25, 50, 150 and 250 mg L^{-1} concentrations (*i.e.*, 33.0 mg g^{-1} for 25 mg L^{-1}, 65.2 mg g^{-1} for 50 mg L^{-1}, 193.5 mg g^{-1} for 150 mg L^{-1}, 301.7 mg g^{-1} for 250 mg L^{-1}) is closer to the experimental values than $q_{e,2}$, as shown in Table 3. The better fit of the Elovich model (≥0.94) at higher CV concentrations suggests that the FCOB surface is heterogeneous, with adsorption occurring on sites of varying energy. This indicates that the adsorption process is chemical in nature, influenced by the activation energy required for chemisorption, similar to observations reported for Cr(VI) adsorption on synthesized biocomposites (cellulose–PLA).[69] The IPD and PFO models exhibited a relatively poorer fit compared to the other kinetic models.

3.8.7. Adsorption isotherm. The Freundlich, Langmuir, Liu, Dubinin-Radushkevitch (D–R), and Temkin models were

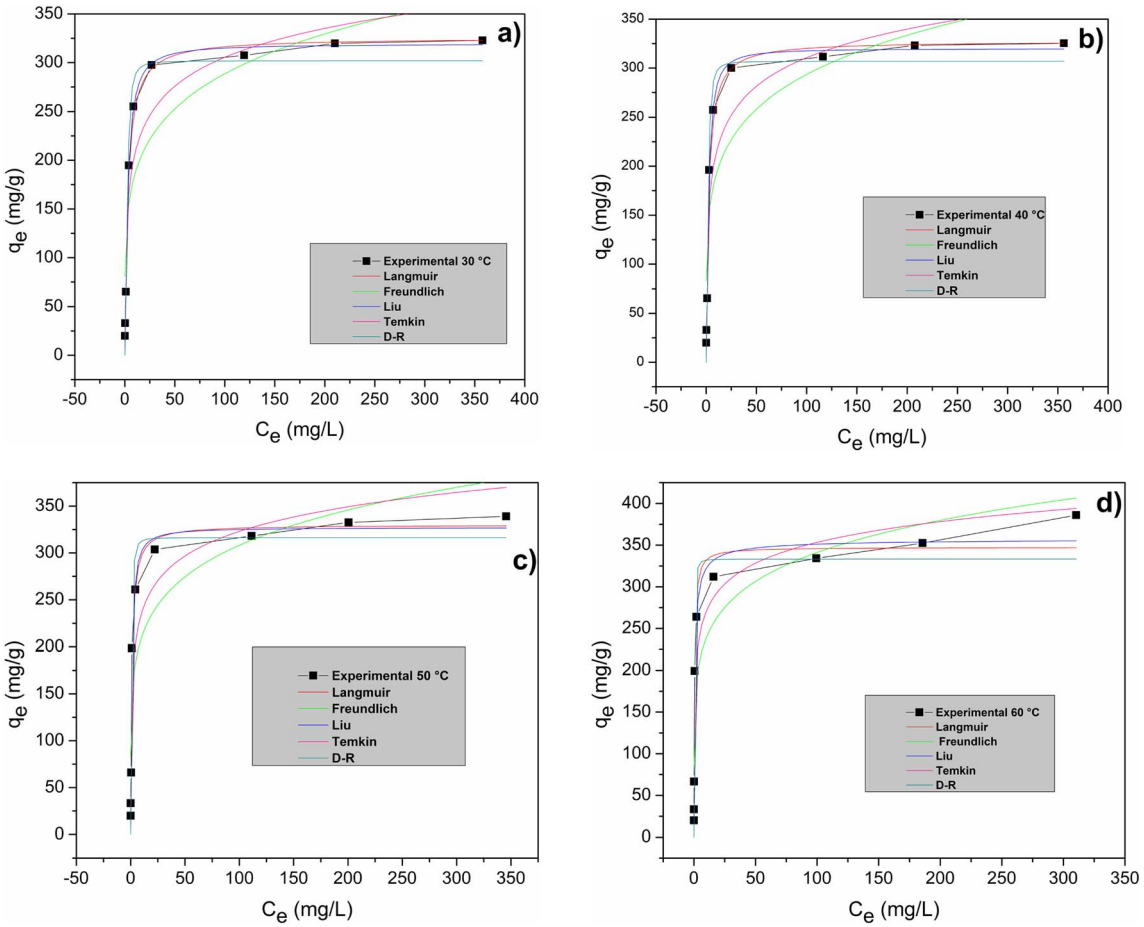

Fig. 11 Nonlinear isotherm fit for the adsorption of CV by FCOB at (a) 30 °C, (b) 40 °C, (c) 50 °C, and (d) 60 °C temperatures [m = 0.03 g, t = 190 min, pH = 8, V = 0.04 L].

Table 4 Adsorption isotherm parameters

		T (°C)			
Model	Parameter	30	40	50	60
Langmuir	q_m (mg g^{-1})	325.5 ± 1.5	327.6 ± 2.4	330.0 ± 3.2	347.4 ± 03.5
	K_L (L mg^{-1})	0.3 ± 0.01	0.4 ± 0.01	0.9 ± 0.019	2.1 ± 0.02
	R^2	0.99	0.98	0.97	0.97
Freundlich	K_F (mg g^{-1} (mg L^{-1})$^{-1/n}$)	119.7 ± 0.5	125.4 ± 0.7	143.1 ± 0.8	167.2 ± 0.9
	n_F	5.2 ± 0.1	5.4 ± 0.5	6.0 ± 0.6	6.4 ± 07
	R^2	0.77 ± 0.15	0.76 ± 0.20	0.78 ± 0.4	0.84 ± 0.6
Liu	q_m (mg g^{-1})	319.2 ± 0.23	319.9 ± 0.35	327.1 ± 0.47	358.2 ± 0.79
	K_g (L mg^{-1})	0.3 ± 0.12	0.4 ± 0.34	0.9 ± 0.45	1.9 ± 056
	n_L	1.20 ± 0.54	1.280 ± 0.52	1.1 ± 0.67	0.74 ± 0.72
	R^2	0.99	0.99	0.96	0.98
Temkin	A_T (L g^{-1})	0.24 ± 0.91	0.34 ± 0.02	0.57 ± 0.37	0.78 ± 0.57
	B (J mol^{-1})	42.8 ± 0.34	42.1 ± 0.56	37.8 ± 0.61	35.9 ± 0.20
	R^2	0.90	0.89	0.90	0.95
DR	q_{max} (mg g^{-1})	301.9 ± 12.7	306.9 ± 10.5	316.3 ± 11.0	333.2 ± 16.1
	β (mol^2 kJ^2)	5.8 ± 1.8	4.0 ± 0.8	1.29 ± 0.2	0.41 ± 0.1
	R^2	0.95	0.96	0.96	0.94

Table 5 $q_{e,exp}$ values for all concentrations at different temperatures

	$q_{e,exp}$ (mg g^{-1}) values at T (°C)			
C_0 (mg L^{-1})	30	40	50	60
15	19.83	19.85	19.94	19.98
25	32.92	32.98	33.22	33.30
50	65.20	65.34	65.96	66.52
150	194.69	196.16	198.53	199.24
200	255.27	257.49	260.97	264.02
250	297.59	300.08	303.68	312.09
350	307.50	311.60	318.15	334.15
450	319.74	323.20	332.59	352.42
600	322.89	325.35	339.09	386.07

Table 6 Thermodynamic parameter ΔG for CV removal by FCOB adsorbent

Temperature (°C)	Temperature (K)	K_g (L mg^{-1})	K (L mol^{-1})	ΔG (kJ mol^{-1})
30	303	0.35	1.42×10^5	−26.85
40	313	0.44	1.79×10^5	−29.36
50	323	0.93	3.79×10^5	−31.86
60	333	1.92	7.83×10^5	−34.37

used to fit (q_e *vs.* C_e)the non-linear data for the isotherm studies at 30°, 40°, 50°, and 60° temperatures. Fig. 11a–d shows the non-linear fitting curves. Table 4 presents the findings of the isotherm parameters. The Langmuir or Liu isotherm model are better-suited model to describe the adsorption of CV on the FCOB adsorbent. The q_{max} values for Langmuir model increase steadily with rising temperature, suggesting that CV adsorption on FCOB surface becomes more favorable at higher temperatures, which again proves the endothermic nature of CV adsorption on FCOB. Similar results have been obtained by Tang *et al.* for the removal of CV by pyrolyzed biochar-based sodium alginate microspheres in which Langmuir q_{max} increases with temperature.[70] At all studied temperatures, the Langmuir model exhibited high R^2 values, confirming that CV adsorption on FCOB occurs predominantly as monolayer coverage on a homogeneous surface. For the Liu model, across the studied temperature range of 30–60 °C, the heterogeneity exponent n_L varied from 0.74 to 1.2. Generally, n_L values close to 1 indicate adsorption on a relatively homogeneous surface, while values <1 reflect surface heterogeneity. So, here, the adsorption is predominantly monolayer and suggests physical adsorption rather than chemisorption.[71] Several authors have raised concerns regarding the correct application of the D–R model to solution–solid adsorption systems, particularly due to the common use of the $1/C_e$ term instead of C_s/C_e.[72,73] In this study, the highest available CR concentration (600 mg L^{-1}) was used as C_s for non-linear fitting, ensuring that $C_s \gg C_e$. D–R model showed the best fit for the adsorption with $R^2 = 1$. The mean adsorption energies calculated from the D–R model at 30, 40, 50, and 60 °C were 0.29, 0.35, 0.62, and 1.1 kJ mol^{-1}, respectively, all well below 8 kJ mol^{-1}. This indicates that the adsorption of CV on FCOB is predominantly governed by physical adsorption, involving weak van der Waals interactions.[74] Thus, the highest D–R model fitting at multiple temperatures allows the estimation of adsorption energies, providing insight into the thermodynamic favorability of the process. The Temkin model showed a slightly good fit with R^2 values >0.88, indicating that adsorbate–adsorbent interactions with a uniform energy distribution contributed to CV adsorption on FCOB; however, the fit was lower than that observed for the Langmuir, Liu, and D–R models. The Freundlich model yielded R^2 values in the range of 0.77–0.80, indicating a moderate fit to the experimental data, suggesting that multilayer adsorption on a heterogeneous surface is less dominant for CV adsorption on FCOB. The $q_{e,exp}$ values for all concentrations are shown in Table 5 at all temperatures for comparison.

3.8.8. Adsorption thermodynamics. By first translating L mg^{-1} into L g^{-1} and then multiplying the result by the molecular weight of the CV (407.9 g mol^{-1}), the value of K_g (L mg^{-1}) was transformed into L mol^{-1}. Using the slope and intercept of the plot of the ln K *versus* $1/T$ (where T is in K) (Fig. S4) and eqn (16), thermodynamic parameters such as enthalpy change (ΔH) and entropy change (ΔS) have been computed. Using eqn (15), the free energy change (ΔG) has been computed (Table 6).

$\Delta H°$ for CV adsorption was positive with a value of 49.03 ± 0.9 kJ mol^{-1} indicating the endothermic nature of adsorption. This is also consistent with increasing R% with increasing temperature. $\Delta S°$ was also positive with a value of 0.25 ± 3.13 kJ mol^{-1} K^{-1}. This indicates increased randomness during CV adsorption on FCOB. The values of $\Delta G°$ for 30 °C, 40 °C, 50 °C, 60 °C were −26.8, −29.3, −31.8, −34.3 kJ mol^{-1} respectively. The negative value of $\Delta G°$ signifies the spontaneity of CV adsorption on FCOB. This means that adsorption occurs on its own (naturally).[32]

3.8.9. ANN investigations. Regression plots are effective tools for evaluating ANN regression performance by comparing predicted outputs with actual (target) values. An R-value close to

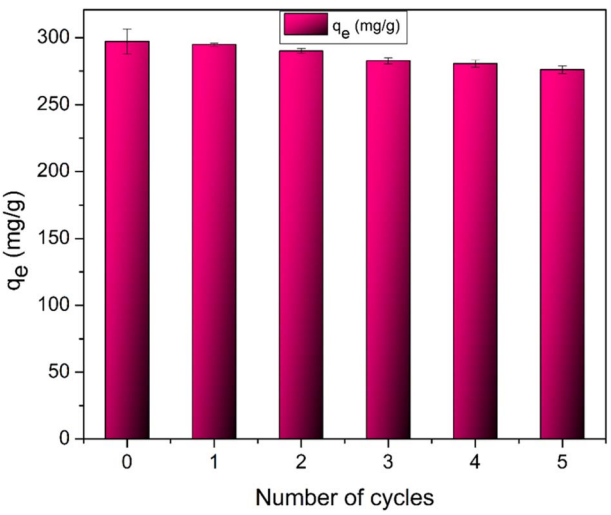

Fig. 12 Regeneration-reuse of FCOB for CV adsorption up to five cycles.

Table 7 Comparison of various biochar adsorbents utilized in the literature for the removal of CV

Biomass	Adsorbent	q_{max} (mg g^{-1})	Reference
Suaeda monoica leaves	FCOB	325.5	Present work
Pine cones	BC/$CoFe_2O_4$@Mn–Fe LDH	41.152	76
C. schweinfurthii stone	CSSB	15.39	77
Palm kernel shell	BC-PKS	24.45	78
Rice husk	XRH	90.02	79
Oil palm frond	OPF biochar	149.03	65
Banana pseudo stem (BPS)	BPS biochar	71.94	80
Murraya koenigii stem	CTC	35.71	81
Melia azedarach seeds	HB-700	209	82
Eucalyptus camaldulensis sawdust	*Eucalyptus camaldulensis* biochar	54.7	83
Date palm petioles	DPP-biochar	209	84

1 indicates that the ANN accurately captured the relationship between inputs and outputs, with most data points aligned along the diagonal. The MSE and R values for ANN-LM and ANN-BR models with varying neuron numbers are presented in Table S2. Performance plots (Fig. S5 and S6) show the variation of MSE with epochs, where the LM and BR models reached stable performance after approximately 25 and 166 epochs, respectively. A decrease in training MSE reflects successful learning, while the lowest MSE indicates optimal performance. Comparison plots of training, validation, and testing data against experimental CV adsorption data are provided in Fig. S7 and S8. The LM algorithm converged faster than BR, requiring fewer epochs. Overall, the ANN was effectively trained to predict adsorption capacity (q) and removal efficiency (%) for CV uptake using FCOB. Both ANN-LM and ANN-BR models demonstrated strong predictive ability across varying conditions of pH, temperature, time, FCOB dosage, and CV concentration.

3.8.10. Regeneration-reuse performance of FCOB. FCOB was regenerated and recycled five times to analyze its stability and recyclability following its initial use. For the 1st cycle, the dye loading on FC-CV was 297.15 mg g^{-1}, and the FCOB was essentially saturated, ensuring that the desorption and subsequent reuse reflected the true regeneration efficiency. Firstly, it was regenerated by washing it with 1 N HCl. CV dye was removed immediately after washing it with the HCl.[75] Rapid removal of CV from the FCOB surface was attributed to the fact that it showed the least CV adsorption (greater than 275 mg g^{-1}) up to five cycles (Fig. 12).

3.8.11. Comparison with other biochar adsorbents. The comparison of present adsorbent FCOB for removal of CV is done with various other biochar adsorbents, given in Table 7. The adsorption capacity of FCOB (325.5 mg g^{-1}) was significantly higher than many reported biochar-based adsorbents for CV, such as CSSB (15.39 mg g^{-1}), BC-PKS (24.45 mg g^{-1}), and Eucalyptus sawdust biochar (54.7 mg g^{-1}). This superior adsorption efficiency highlights the effectiveness of ferrite modification in enhancing the surface functionality and adsorption sites of biochar for CV removal.

4. Conclusions

The CV adsorption capability of the FCOB composite was thoroughly examined in this work. Ferrite spinel was successfully incorporated, as evidenced by EDS analysis. In alkaline pHs, the CV adsorption was favourable by FCOB. High adsorption occurred at pH 8 due to a strong adsorption affinity between CV and FCOB. The composite's best adsorption performance was achieved at pH 8, with CV C_0 = 250 mg L^{-1}, a dosage of 30 mg of FCOB, and a minimum contact period of 120 minutes. With negative ΔG^0, which indicates spontaneous absorption of CV by FCOB, the adsorption was favourable at high temperatures. FCOB maintained an adsorption capacity of >200 mg g^{-1} even after five regeneration–reuse cycles. The isotherm data fit well with the Langmuir, Liu, and D–R isotherm models. A maximum Langmuir adsorption capacity of 325.5 mg g^{-1} at 30 °C underscores the composite's strong affinity for CV, suggesting a monolayer adsorption. The best fit of Pseudo-second-order kinetic modeling revealed that chemisorption controls the adsorption of CV onto FCOB. The adsorption mechanism of CV, as identified by FTIR, involves hydrogen bonding, π–π interactions, electrostatic attraction, and surface complexation, corroborated by zeta potential data indicating an electrostatic contribution. Furthermore, ANN analysis showed that both BR and LM algorithms effectively predicted removal efficiency and adsorption capacity (R value > 0.99). Overall, the FCOB composite is a promising, reusable, and scalable adsorbent for CV removal. However, its relatively slow adsorption rate presents a limitation, warranting further optimization in future research.

Author contributions

Disha Mehta: writing – original draft, methodology, investigation, formal analysis, data curation. Pragnesh N. Dave: writing – review & editing, resources. V. Vijaykumar: resources.

Conflicts of interest

The authors declare that they have no known competing financial interests or personal relationships that could have appeared to influence the work reported in this paper.

Data availability

The data supporting the study's conclusions are attached in SI file. See DOI: **https://doi.org/10.1039/d5ra04604a**.

Acknowledgements

The authors are grateful to UGC-CPEPA and UGC, New Delhi for UGC-CAS-phase-II (F947 540/5/CAS-II/2018 (SAP-I)) for providing chemical facilities and UGC-CPEPA for AFM, TGA and FT-IR facility. The authors acknowledge the research and instrumentation facilities provided by the Department of Chemistry, Sardar Patel University. The XRD investigation was conducted at the Department Of Physics, Sardar Patel University, Anand. SEM and EDX analyses were conducted at SICART, Sardar Patel University, Anand and IIT Gandhinagar institutes. The authors thank IICISST, Vallabh Vidyanagar for DLS measurement. DM is grateful to "Scheme of Developing High Quality Research (SHODH)", India, for Shodh fellowship, File No. 202301642 dated 21-01-2025.

References

1 G. K. Cheruiyot, W. C. Wanyonyi, J. J. Kiplimo and E. N. Maina, Adsorption of Toxic Crystal Violet Dye Using Coffee Husks: Equilibrium, Kinetics and Thermodynamics Study, *Sci. Afr.*, 2019, **5**, e00116, DOI: **10.1016/j.sciaf.2019.e00116**.

2 S. Gul, S. Afsar, H. Gul and B. Ali, Removal of Crystal Violet Dye from Wastewater Using Low-Cost Biosorbent Trifolium Repens Stem Powder, *J. Iran. Chem. Soc.*, 2023, **20**(11), 2781–2792, DOI: **10.1007/s13738-023-02875-x**.

3 A. Mirza and R. Ahmad, An Efficient Sequestration of Toxic Crystal Violet Dye from Aqueous Solution by Alginate/Pectin Nanocomposite: A Novel and Ecofriendly Adsorbent, *Groundwater Sustainable Dev.*, 2020, **11**, 100373, DOI: **10.1016/j.gsd.2020.100373**.

4 D. Gu, K. Andreev and M. E. Dupre, Major Trends in Population Growth Around the World, *China CDC Wkly.*, 2021, **3**(28), 604–613, DOI: **10.46234/ccdcw2021.160**.

5 S. Mishra and B. Sundaram, A Review of the Photocatalysis Process Used for Wastewater Treatment, *Mater. Today: Proc.*, 2024, **102**, 393–409, DOI: **10.1016/j.matpr.2023.07.147**.

6 X. Wu, Y. Lin, Z. Pi and X. Tan, Dual-functional Fe@ZIF-8 for Efficient Phosphite Removal from Wastewater: Synergistic Peroxymonosulfate Activation and Adsorption, *Sep. Purif. Technol.*, 2025, **377**, 134236.

7 M. D. Khan, A. Singh, M. Z. Khan, S. Tabraiz and J. Sheikh, Current Perspectives, Recent Advancements, and Efficiencies of Various Dye-Containing Wastewater Treatment Technologies, *J. Water Process Eng.*, 2023, **53**, 103579, DOI: **10.1016/j.jwpe.2023.103579**.

8 K. H. D. Tang, N. M. Darwish, A. M. Alkahtani, M. R. AbdelGawwad and P. Karácsony, Biological Removal of Dyes from Wastewater: A Review of Its Efficiency and Advances, *Trop. Aquat. Soil Pollut.*, 2022, **2**(1), 59–75, DOI: **10.53623/tasp.v2i1.72**.

9 J. S. Sravan, L. Matsakas and O. Sarkar, Advances in Biological Wastewater Treatment Processes: Focus on Low-Carbon Energy and Resource Recovery in Biorefinery Context, *Bioengineering*, 2024, **11**(3), 281, DOI: **10.3390/bioengineering11030281**.

10 B. Mulla, K. Ioannou, G. Kotanidis, I. Ioannidis, G. Constantinides, M. Baker, S. Hinder, C. Mitterer, I. Pashalidis, N. Kostoglou and C. Rebholz, Removal of Crystal Violet Dye from Aqueous Solutions through Adsorption onto Activated Carbon Fabrics, *C*, 2024, **10**(1), 19, DOI: **10.3390/c10010019**.

11 Z. Falaki and H. Bashiri, Preparing an Adsorbent from the Unused Solid Waste of Rosewater Extraction for High Efficient Removal of Crystal Violet, *J. Iran. Chem. Soc.*, 2021, **18**(10), 2689–2702, DOI: **10.1007/s13738-021-02222-y**.

12 S. Jana, M. K. Purkait and K. Mohanty, Removal of Crystal Violet by Advanced Oxidation and Microfiltration, *Appl. Clay Sci.*, 2010, **50**(3), 337–341, DOI: **10.1016/j.clay.2010.08.023**.

13 G. Crini and E. Lichtfouse, Advantages and Disadvantages of Techniques Used for Wastewater Treatment, *Environ. Chem. Lett.*, 2019, **17**(1), 145–155, DOI: **10.1007/s10311-018-0785-9**.

14 S. Ho, Low-Cost Adsorbents for the Removal of Phenol/Phenolics, Pesticides, and Dyes from Wastewater Systems: A Review, *Water*, 2022, **14**(20), 3203, DOI: **10.3390/w14203203**.

15 M. Ait Haki, A. Imgharn, N. Aarab, A. Hsini, A. Essekri, M. Laabd, H. El Jazouli, M. Elamine, R. Lakhmiri and A. Albourine, Efficient Removal of Crystal Violet Dye from Aqueous Solutions Using Sodium Hydroxide-Modified Avocado Shells: Kinetics and Isotherms Modeling, *Water Sci. Technol.*, 2022, **85**(1), 433–448, DOI: **10.2166/wst.2021.451**.

16 O. O. Oluwasina, A. A. Adelodun, O. O. Oluwasina, H. A. Duarte and S. J. Olusegun, Experimental and Computational Studies of Crystal Violet Removal from Aqueous Solution Using Sulfonated Graphene Oxide, *Sci. Rep.*, 2024, **14**(1), 6207, DOI: **10.1038/s41598-024-54499-7**.

17 I. Bougdah, S. Bouasla, W. Mecibah, C. Sobhi, M. Cherifi, M. Najran, D. Bousba and A. Zeglil, Crystal Violet Removal from Aqueous Solution Using Urtica dioica Leaves Powder as a Low-Cost Natural Adsorbent: Isotherm, Kinetics and Thermodynamics Studies, *Chem. Afr.*, 2023, **7**(2), 915–928.

18 R. Sirach and P. N. Dave, Artificial Neural Network Modelling and Experimental Investigations of Malachite Green Adsorption on Novel Carboxymethyl Cellulose/β-Cyclodextrin/Nickel Cobaltite Composite, *Heliyon*, 2024, **10**(13), e33820, DOI: **10.1016/j.heliyon.2024.e33820**.

19 M. Xiao, H.-D. Yue, X.-J. Feng, Y.-T. Wang, M.-Y. He, Q. Chen and Z.-H. Zhang, A Double-Layered Neutral Cadmium-Organic Framework for Selective Adsorption of Cationic Organic Dyes through Electrostatic Affinity, *J. Solid State Chem.*, 2020, **288**, 121376, DOI: **10.1016/j.jssc.2020.121376**.

20 R. Sirach and P. N. Dave, *β -Cyclodextrin* Polymer/Zinc Ferrite Nanocomposite: Synthesis, Characterization, and Adsorption Application for the Removal of Malachite Green and Congo Red, *J. Hazard. Mater. Adv.*, 2023, **10**, 100300, DOI: **10.1016/j.hazadv.2023.100300**.

21 Biochar and its Application, **https://www.researchgate.net/publication/344138848_Biochar_and_its_Application**, accessed 2025-08-24.

22 P. Sun, C. Hui, R. Azim Khan, J. Du, Q. Zhang and Y.-H. Zhao, Efficient Removal of Crystal Violet Using Fe3O4-Coated Biochar: The Role of the Fe3O4 Nanoparticles and Modeling Study Their Adsorption Behavior, *Sci. Rep.*, 2015, **5**(1), 12638, DOI: 10.1038/srep12638.

23 B. Yao, Y. Li, W. Zeng, G. Yang, J. Zeng, J. Nie and Y. Zhou, Synergistic Adsorption and Oxidation of Trivalent Antimony from Groundwater Using Biochar Supported Magnesium Ferrite: Performances and Mechanisms, *Environ. Pollut.*, 2023, **323**, 121318.

24 S. Perveen, R. Nadeem, F. Nosheen, M. I. Asjad, J. Awrejcewicz and T. Anwar, Biochar-Mediated Zirconium Ferrite Nanocomposites for Tartrazine Dye Removal from Textile Wastewater, *Nanomaterials*, 2022, **12**(16), 2828, DOI: 10.3390/nano12162828.

25 S. A. Rashdan and L. J. Hazeem, Synthesis of Spinel Ferrites Nanoparticles and Investigating Their Effect on the Growth of Microalgae *Picochlorum Sp.*, *Arab J. Basic Appl. Sci.*, 2020, **27**(1), 134–141, DOI: 10.1080/25765299.2020.1733174.

26 X. Li, C. Wang, J. Zhang, J. Liu, B. Liu and G. Chen, Preparation and Application of Magnetic Biochar in Water Treatment: A Critical Review, *Sci. Total Environ.*, 2020, **711**, 134847, DOI: 10.1016/j.scitotenv.2019.134847.

27 R. Kareem, A. Afkhami and K. H. Hama Aziz, Synthesis of a Novel Magnetic Biochar Composite Enhanced with Polyaniline for High-Performance Adsorption of Heavy Metals: Focus on Hg(ii) and Cu(ii), *RSC Adv.*, 2025, **15**(25), 20309–20320, DOI: 10.1039/D5RA02250A.

28 M. S. Al-Said, N. A. Siddiqui, M. A. Mukhair, M. K. Parvez, P. Alam, M. Ali and A. Haque, A Novel Monocyclic Triterpenoid and a Norsesquaterpenol from the Aerial Parts of Suaeda Monoica Forssk. Ex J.F. Gmel with Cell Proliferative Potential, *Saudi Pharm. J.*, 2017, **25**(7), 1005–1010, DOI: 10.1016/j.jsps.2017.03.008.

29 J. López-Luna, L. E. Ramírez-Montes, S. Martinez-Vargas, A. I. Martínez, O. F. Mijangos-Ricardez, M. D. C. A. González-Chávez, R. Carrillo-González, F. A. Solís-Domínguez, M. D. C. Cuevas-Díaz and V. Vázquez-Hipólito, Linear and Nonlinear Kinetic and Isotherm Adsorption Models for Arsenic Removal by Manganese Ferrite Nanoparticles, *SN Appl. Sci.*, 2019, **1**(8), 950, DOI: 10.1007/s42452-019-0977-3.

30 A. Goel, A. K. Goel and A. Kumar, The Role of Artificial Neural Network and Machine Learning in Utilizing Spatial Information, *Spat. Inf. Res.*, 2023, **31**(3), 275–285, DOI: 10.1007/s41324-022-00494-x.

31 F. Amato, A. López, E. M. Peña-Méndez, P. Vaňhara, A. Hampl and J. Havel, Artificial Neural Networks in Medical Diagnosis, *J. Appl. Biomed.*, 2013, **11**(2), 47–58, DOI: 10.2478/v10136-012-0031-x.

32 P. S. Pauletto, S. F. Lütke, G. L. Dotto and N. P. G. Salau, Forecasting the Multicomponent Adsorption of Nimesulide and Paracetamol through Artificial Neural Network, *Chem. Eng. J.*, 2021, **412**, 127527, DOI: 10.1016/j.cej.2020.127527.

33 M. S. B. Maind and M. P. Wankar, Research Paper on Basic of Artificial Neural Network, *Int. J. Recent Innov. Trends Comput. Commun.*, 2014, **2**(1), 96–100, DOI: 10.17762/ijritcc.v2i1.2920.

34 R. Lafi, I. Montasser and A. Hafiane, Adsorption of Congo Red Dye from Aqueous Solutions by Prepared Activated Carbon with Oxygen-Containing Functional Groups and Its Regeneration, *Adsorpt. Sci. Technol.*, 2018, **37**, 160–181, DOI: 10.1177/0263617418819227.

35 S. Sun, Y. Zhu, Z. Gu, H. Chu, C. Hu, L. Gao and X. Zhao, Adsorption of Crystal Violet on Activated Bamboo Fiber Powder from Water: Preparation, Characterization, Kinetics and Isotherms, *RSC Adv.*, 2023, **13**(9), 6108–6123, DOI: 10.1039/D2RA08323J.

36 R. Sirach and P. N. Dave, ZnO Reinforced Carboxymethyl Cellulose/β-Cyclodextrin Nanocomposite for Malachite Green Adsorption: Isotherm, Kinetics, and Thermodynamic Evaluation, *Cellulose*, 2025, **32**, 5647–5673, DOI: 10.1007/s10570-025-06586-9.

37 C. G. Sonwane and S. K. Bhatia, Characterization of Pore Size Distributions of Mesoporous Materials from Adsorption Isotherms, *J. Phys. Chem. B*, 2000, **104**(39), 9099–9110, DOI: 10.1021/jp000907j.

38 W. Jiang, Y. Cai, D. Liu, X. Yu and Q. Wang, Enhanced Adsorption Performance of Oxytetracycline in Aqueous Solutions by Mg-Fe Modified Suaeda-Based Magnetic Biochar, *Environ. Res.*, 2024, **241**, 117662, DOI: 10.1016/j.envres.2023.117662.

39 W. Jiang, Y. Cai, D. Liu, Q. Shi and Q. Wang, Adsorption properties and mechanism of suaeda biochar and modified materials for tetracycline, *Environ. Res.*, 2023, **235**, DOI: 10.1016/j.envres.2023.116549.

40 M. Rabiei, A. Palevicius, A. Dashti, S. Nasiri, A. Monshi, A. Vilkauskas and G. Janusas, Measurement Modulus of Elasticity Related to the Atomic Density of Planes in Unit Cell of Crystal Lattices, *Materials*, 2020, **13**(19), 4380, DOI: 10.3390/ma13194380.

41 M. A. Hassaan, M. Yılmaz, M. Helal, M. A. El-Nemr, S. Ragab and A. El Nemr, Isotherm and Kinetic Investigations of Sawdust-Based Biochar Modified by Ammonia to Remove Methylene Blue from Water, *Sci. Rep.*, 2023, **13**, 12724, DOI: 10.1038/s41598-023-39971-0.

42 K. Sadhana, K. Praveena, S. Bharadwaj and S. R. Murthy, Microwave-Hydrothermal Synthesis of BaTiO3+NiCuZnFe2O4 Nanocomposites, *J. Alloys Compd.*, 2009, **472**(1–2), 484–488, DOI: 10.1016/j.jallcom.2008.04.104.

43 H. Cai, Q. Wei, H. Xiao, H. Liu and J. Wang, Preparation and Microwave Absorption Properties of Petal CoO/CNFs Composites, *J. Mater. Sci.: Mater. Electron.*, 2020, **31**(10), 7606–7615, DOI: 10.1007/s10854-020-03231-y.

44 W.-H. Huang, R.-M. Wu, J.-S. Chang, S.-Y. Juang and D.-J. Lee, Pristine and Manganese Ferrite Modified Biochars for Copper Ion Adsorption: Type-Wide Comparison, *Bioresour. Technol.*, 2022, **360**, 127529, DOI: 10.1016/j.biortech.2022.127529.

45 Y. Ikemoto, Y. Harada, M. Tanaka, S. Nishimura, D. Murakami, N. Kurahashi, T. Moriwaki, K. Yamazoe, H. Washizu, Y. Ishii and H. Torii, Infrared Spectra and Hydrogen-Bond Configurations of Water Molecules at the

Interface of Water-Insoluble Polymers under Humidified Conditions, *J. Phys. Chem. B*, 2022, **126**(22), 4143–4151, DOI: 10.1021/acs.jpcb.2c01702.

46 K. Chen, Y. Zhang, C. Liu, Y. Zhang and X. Zhang, The Evolution of Structure and Properties in High-Tenacity Poly(Ethylene Terephthalate) Industrial Fibers during Thermal-Oxidative Aging Process, *Polymer*, 2024, **307**, 127246, DOI: 10.1016/j.polymer.2024.127246.

47 Á. V. Delgado, F. González-Caballero, R. J. Hunter, L. K. Koopal and J. Lyklema, Measurement and Interpretation of Electrokinetic Phenomena, *J. Colloid Interface Sci.*, 2007, **309**(2), 194–224.

48 S. Guilhen, T. Watanabe, T. Silva, S. Rovani, J. Marumo, J. Tenório, O. Masek and L. de Araujo, Role of Point of Zero Charge in the Adsorption of Cationic Textile Dye on Standard Biochars from Aqueous Solutions: Selection Criteria and Performance Assessment, *Recent Prog. Mater.*, 2022, **4**, 1, DOI: 10.21926/rpm.2202010.

49 S. Wang, F. Sadegh-Zadeh and B. Jalili, Adsorption of As(III) and As(V) by Fe Coated Biochars and Biochars Produced from Empty Fruit Bunch and Rice Husk, *J. Environ. Chem. Eng.*, 2013, **1**, 981–988, DOI: 10.1016/j.jece.2013.08.009.

50 F. Chen, Y. Sun, C. Liang, T. Yang, S. Mi, Y. Dai, M. Yu and Q. Yao, Adsorption Characteristics and Mechanisms of Cd2+ from Aqueous Solution by Biochar Derived from Corn Stover, *Sci. Rep.*, 2022, **12**, 17714, DOI: 10.1038/s41598-022-22714-y.

51 H. Yang, R. Yan, H. Chen, D. H. Lee and C. Zheng, Characteristics of Hemicellulose, Cellulose and Lignin Pyrolysis, *Fuel*, 2007, **86**(12–13), 1781–1788, DOI: 10.1016/j.fuel.2006.12.013.

52 S. A. El-Sayed, T. M. Khass and M. E. Mostafa, Thermal Degradation Behaviour and Chemical Kinetic Characteristics of Biomass Pyrolysis Using TG/DTG/DTA Techniques, *Biomass Convers. Biorefin.*, 2024, **14**(15), 17779–17803, DOI: 10.1007/s13399-023-03926-2.

53 W. O. D. Souza, K. Garcia, C. F. D. A. Von Dollinger and L. C. Pardini, Electrical Behavior of Carbon Fiber/Phenolic Composite during Pyrolysis, *Mater. Res.*, 2015, **18**(6), 1209–1216, DOI: 10.1590/1516-1439.000515.

54 W. F. Da Silva Júnior, J. G. D. O. Pinheiro, C. D. L. Moreira, A. L. Rüdiger, E. G. Barbosa, E. S. Lima, V. F. Da Veiga Júnior, A. A. Da Silva Júnior, C. F. S. Aragão and Á. A. N. De Lima, Thermal Behavior and Thermal Degradation Kinetic Parameters of Triterpene α, β Amyrin, *J. Therm. Anal. Calorim.*, 2017, **127**(2), 1757–1766, DOI: 10.1007/s10973-016-6046-x.

55 M. Latos-Brozio, A. Masek and M. Piotrowska, Effect of Enzymatic Polymerization on the Thermal Stability of Flavonoids, *J. Therm. Anal. Calorim.*, 2023, **148**(12), 5357–5374, DOI: 10.1007/s10973-023-12089-1.

56 B. Tisserat, R. H. O'kuru, H. Hwang, A. A. Mohamed and R. Holser, Glycerol Citrate Polyesters Produced through Heating without Catalysis, *J. Appl. Polym. Sci.*, 2012, **125**(5), 3429–3437, DOI: 10.1002/app.36669.

57 E. Apaydın Varol and Ü. Mutlu, TGA-FTIR Analysis of Biomass Samples Based on the Thermal Decomposition Behavior of Hemicellulose, Cellulose, and Lignin, *Energies*, 2023, **16**(9), 3674, DOI: 10.3390/en16093674.

58 R. Panizio, C. Castro, N. Pacheco, A. C. Assis, A. Longo, C. Vilarinho, J. C. Teixeira, P. Brito, M. Gonçalves and C. Nobre, Investigation of Biochars Derived from Waste Lignocellulosic Biomass and Insulation Electric Cables: A Comprehensive TGA and Macro-TGA Analysis, *Heliyon*, 2024, **10**(18), e37882, DOI: 10.1016/j.heliyon.2024.e37882.

59 A. K. Sakhiya, A. Anand and P. Kaushal, Production, Activation, and Applications of Biochar in Recent Times, *Biochar*, 2020, **2**(3), 253–285, DOI: 10.1007/s42773-020-00047-1.

60 Z. Guo, G. Bai, B. Huang, N. Cai, P. Guo and L. Chen, Preparation and Application of a Novel Biochar-Supported Red Mud catalyst:Active Sites and Catalytic Mechanism, *J. Hazard. Mater.*, 2021, **408**, 124802, DOI: 10.1016/j.jhazmat.2020.124802.

61 A. Bardaoui, H. Abdelli, A. Siai and I. Ben Assaker, Evaluation of Spinel Ferrites MFe2O4 (M = Cu, Ni, Zn, and Co) Photocatalytic Properties in Selective Dehydrogenation of Formic Acid Towards Hydrogen Production, *Catal. Lett.*, 2025, **155**(5), 164, DOI: 10.1007/s10562-025-05007-7.

62 S. V. Vassilev, D. Baxter, L. K. Andersen, C. G. Vassileva and T. J. Morgan, An Overview of the Organic and Inorganic Phase Composition of Biomass, *Fuel*, 2012, **94**, 1–33, DOI: 10.1016/j.fuel.2011.09.030.

63 M. Abdi, M. Balagabri, H. Karimi, H. Hossini and S. O. Rastegar, Degradation of Crystal Violet (CV) from Aqueous Solutions Using Ozone, Peroxone, Electroperoxone, and Electrolysis Processes: A Comparison Study, *Appl. Water Sci.*, 2020, **10**(7), 168, DOI: 10.1007/s13201-020-01252-w.

64 A. Wathukarage, I. Herath, M. C. M. Iqbal and M. Vithanage, Mechanistic Understanding of Crystal Violet Dye Sorption by Woody Biochar: Implications for Wastewater Treatment, *Environ. Geochem. Health*, 2019, **41**(4), 1647–1661, DOI: 10.1007/s10653-017-0013-8.

65 A. A. Oyekanmi, K. K. Katibi, R. C. Omar, A. Ahmad, M. Elbidi, M. B. Alshammari and I. G. Shitu, A Novel Oil Palm Frond Magnetic Biochar for the Efficient Adsorption of Crystal Violet and Sunset Yellow Dyes from Aqueous Solution: Synthesis, Kinetics, Isotherm, Mechanism and Reusability Studies, *Appl. Water Sci.*, 2024, **14**(2), 13, DOI: 10.1007/s13201-023-02060-8.

66 E. Rápó and S. Tonk, Factors Affecting Synthetic Dye Adsorption; Desorption Studies: A Review of Results from the Last Five Years (2017–2021), *Molecules*, 2021, **26**(17), 5419, DOI: 10.3390/molecules26175419.

67 M. Zeeshan, T. Javed, C. Kumari, A. Thumma, M. Wasim, M. B. Taj, I. Sharma, M. N. Haider and M. Batool, Investigating the Interactions between Dyes and Porous/Composite Materials: A Comprehensive Study, *Sustain. Chem. Environ.*, 2025, **9**, 100217, DOI: 10.1016/j.scenv.2025.100217.

68 N. E. Brichi, F. Z. Batana, M. Djedid, R. Hadjaissa, N. Bouzar and M. Benalia, Mechanistic Insights into Crystal Violet Adsorption: A Comparative Study of Raw Bentonite and γ-

Fe2O3/Bentonite Magnetic Composite, *React. Kinet., Mech. Catal.*, 2025, **134**, 427–442, DOI: **10.1007/s11144-025-02940-x**.

69 C. Tejada-Tovar, Á. Villabona-Ortiz and R. Ortega-Toro, Kinetic, Isothermal and Thermodynamic Study on the Removal of Hexavalent Chromium with Biocomposites (Cellulose–PLA), *J. Compos. Sci.*, 2025, **9**(1), 36, DOI: **10.3390/jcs9010036**.

70 L. Tang, C. Liu, X. Liu, L. Zhang, B. Fan, B. Wang and F. Wang, Efficient Adsorption of Crystal Violet by Different Temperature Pyrolyzed Biochar-Based Sodium Alginate Microspheres: A Green Solution for Food Industry Dye Removal, *Food Chem.: X*, 2025, **26**, 102311, DOI: **10.1016/j.fochx.2025.102311**.

71 É. C. Lima, M. A. Adebayo and F. M. Machado, Kinetic and Equilibrium Models of Adsorption, in *Carbon Nanomaterials as Adsorbents for Environmental and Biological Applications*, ed. Bergmann, C. P. and Machado, F. M., Carbon Nanostructures, Springer International Publishing, Cham, 2015, pp. 33–69, DOI: **10.1007/978-3-319-18875-1_3**.

72 B. Mahanty, S. K. Behera and N. K. Sahoo, Misinterpretation of Dubinin–Radushkevich Isotherm and Its Implications on Adsorption Parameter Estimates, *Sep. Sci. Technol.*, 2023, **58**(7), 1275–1282, DOI: **10.1080/01496395.2023.2189050**.

73 Q. Hu and Z. Zhang, Application of Dubinin–Radushkevich Isotherm Model at the Solid/Solution Interface: A Theoretical Analysis, *J. Mol. Liq.*, 2019, **277**, 646–648, DOI: **10.1016/j.molliq.2019.01.005**.

74 C. R. Girish, Determination of Thermodynamic Parameters in Adsorption Studies: A Review, *Chem. Pap.*, 2025, **79**(9), 5687–5706, DOI: **10.1007/s11696-025-04218-x**.

75 W. Xu, B. Cai, X. Zhang, Y. Zhang, Y. Zhang and H. Peng, The Biochar Derived from Pecan Shells for the Removal of Congo Red: The Effects of Temperature and Heating Rate, *Molecules*, 2024, **29**(23), 5532, DOI: **10.3390/molecules29235532**.

76 S. J. Peighambardoust, S. Abdollahian Aghbolagh, R. Foroutan and N. S. Peighambardoust, Decontamination of Crystal Violet Using Nanocomposite Adsorbent Based on Pine Cone Biochar Modified with CoFe2O4/Mn-Fe LDH, *Sci. Rep.*, 2025, **15**(1), 15067, DOI: **10.1038/s41598-025-99549-w**.

77 M. O. Ani, M. C. Menkiti, C. O. Aniagor, C. E. Nworie and D. O. Ochi, *Canarium Schweinfurthii* Stone-Derived Biochar: A Promising Adsorbent for Crystal Violet Dye Removal, *Results Surf. Interfaces*, 2023, **12**, 100144, DOI: **10.1016/j.rsurfi.2023.100144**.

78 P. P. Kyi, J. O. Quansah, C.-G. Lee, J.-K. Moon and S.-J. Park, The Removal of Crystal Violet from Textile Wastewater Using Palm Kernel Shell-Derived Biochar, *Appl. Sci.*, 2020, **10**(7), 2251, DOI: **10.3390/app10072251**.

79 P. L. Homagai, R. Poudel, S. Poudel and A. Bhattarai, Adsorption and Removal of Crystal Violet Dye from Aqueous Solution by Modified Rice Husk, *Heliyon*, 2022, **8**(4), e09261, DOI: **10.1016/j.heliyon.2022.e09261**.

80 F. Sjahrir, R. Mohd Taib, I. Norazlina, N. Baharim and T. Tuan Daud, Comparison of Biosorbent and Biochar Derived from Banana Pseudo Stem Waste for Crystal Violet Removal from Synthetic Wastewater, *Sci. Technol. Asia*, 2024, **29**(3), 25–35.

81 A. Saniya, K. Sathya, K. Nagarajan, M. Yogesh, H. Jayalakshmi, P. Praveena and S. Bharathi, Modelling of the Removal of Crystal Violet Dye from Textile Effluent Using Murraya Koenigii Stem Biochar, *Desalin. Water Treat.*, 2020, **203**, 356–365, DOI: **10.5004/dwt.2020.26191**.

82 A. Nouioua, D. Ben Salem, A. Ouakouak, N. Rouahna, O. Baigenzhenov and A. Hosseini-Bandegharaei, Production of Biochar from Melia Azedarach Seeds for the Crystal Violet Dye Removal from Water: Combining of Hydrothermal Carbonization and Pyrolysis, *Bioengineered*, 2023, **14**(1), 290–306, DOI: **10.1080/21655979.2023.2236843**.

83 M. T. Amin, A. A. Alazba and M. Shafiq, Successful Application of Eucalyptus Camdulensis Biochar in the Batch Adsorption of Crystal Violet and Methylene Blue Dyes from Aqueous Solution, *Sustainability*, 2021, **13**(7), 3600, DOI: **10.3390/su13073600**.

84 H.-O. Chahinez, O. Abdelkader, Y. Leila and H. N. Tran, One-Stage Preparation of Palm Petiole-Derived Biochar: Characterization and Application for Adsorption of Crystal Violet Dye in Water, *Environ. Technol. Innovation*, 2020, **19**, 100872, DOI: **10.1016/j.eti.2020.100872**.